

## Conjoint specification of action by neocortex and striatum

### Highlights

- A task to study how mice select between reach-to-pull actions with distinct kinematics
- Simultaneous recording reveals distributed cortical/subcortical encoding of action
- Cortex and striatum population activity together determines action parameters
- Striatum has greater spatial and temporal distribution of movement kinematic encoding

### Authors

Junchol Park, Peter Polidoro,  
Catia Fortunato, Jon Arnold,  
Brett Mensh, Juan A. Gallego,  
Joshua T. Dudman

### Correspondence

parkj.learning@gmail.com (J.P.),  
dudmanj@janelia.hhmi.org (J.T.D.)

### In brief

Park et al. show that motor cortex and subcortical striatum act in concert to specify the movement parameters of a reach-to-pull action in mice.



Article

# Conjoint specification of action by neocortex and striatum

Junchol Park,<sup>1,\*</sup> Peter Polidoro,<sup>1</sup> Catia Fortunato,<sup>2</sup> Jon Arnold,<sup>1</sup> Brett Mensh,<sup>1</sup> Juan A. Gallego,<sup>2</sup> and Joshua T. Dudman<sup>1,3,\*</sup>

<sup>1</sup>Janelia Research Campus, Howard Hughes Medical Institute, Ashburn, VA 20147, USA

<sup>2</sup>Department of Bioengineering, Imperial College London, London W12 0BZ, UK

<sup>3</sup>Lead contact

\*Correspondence: parkj.learning@gmail.com (J.P.), dudmanj@janelia.hhmi.org (J.T.D.)

<https://doi.org/10.1016/j.neuron.2024.12.024>

## SUMMARY

The interplay between two major forebrain structures—cortex and subcortical striatum—is critical for flexible, goal-directed action. Traditionally, it has been proposed that striatum is critical for selecting what type of action is initiated, while the primary motor cortex is involved in specifying the continuous parameters of an upcoming/ongoing movement. Recent data indicate that striatum may also be involved in specification. These alternatives have been difficult to reconcile because comparing very distinct actions, as is often done, makes essentially indistinguishable predictions. Here, we develop quantitative models to reveal a somewhat paradoxical insight: only comparing neural activity across similar actions makes strongly distinguishing predictions. We thus developed a novel reach-to-pull task in which mice reliably selected between two similar but distinct reach targets and pull forces. Simultaneous cortical and subcortical recordings were uniquely consistent with a model in which cortex and striatum jointly specify continuous parameters governing movement execution.

## INTRODUCTION

Mammals have multi-jointed limbs with many degrees of freedom, enabling highly flexible, complex, and dexterous actions. It has long been appreciated that these many degrees of freedom pose daunting control challenges for the nervous system.<sup>1</sup> For an animal to successfully reach out to grasp a piece of food, the forelimb can take numerous trajectories, each implemented by a complex pattern of activation across many muscles. While our understanding of the processes underlying the planning and execution of actions is understandably incomplete, a number of principles and a relatively detailed outline have emerged.<sup>2–5</sup> The canonical functional sequence requires a target to be chosen, which is converted via a sensorimotor transform into egocentric coordinates; an effector to be selected and a kinematic trajectory to be planned; followed by online control of movement execution. In a reach-to-grasp action, this sequence might involve identifying the location of a piece of food, computing a vector from the current hand location to the food, choosing to reach from below to avoid an obstacle, and reaching slowly with high co-contraction to accurately grasp the food. One principled distinction in these functional processes is between “selection” operations that reduce a set of discrete possibilities to a single option and “specification” operations that set continuous parameters governing execution.<sup>2,4,6</sup> For example, one may select which piece of food to target or which forelimb to use, in distinction from specifying a particular speed of movement or tightness of grasp.

Seminal work has mapped this abstract motor planning and execution sequence onto a distributed and partially dissociable set of brain areas thought to implement these functional processes.<sup>7</sup> For example, in the neocortex, the selection of a target and transformation into egocentric coordinates during motor planning map well onto posterior parietal cortical areas.<sup>3</sup> Action selection (effector and target) maps onto processes in premotor areas in the medial wall of frontal cortex such as anterior cingulate area (ACA) in the primate<sup>2,4,5,8</sup> and likely onto homologous areas of cingulate and secondary motor cortex (MOs) in rodents.<sup>9</sup> Action specification, in distinction, maps onto the primary motor cortex (MOp).<sup>10–13</sup> One particularly strong piece of evidence for specification in MOp is that its activity explains more of the variance in movement trajectories (kinematics) and forces (kinetics) than cingulate areas.<sup>8</sup> Moreover, disruption of MOp function can produce profound deficits in voluntary forelimb control as expected from its dense projections to spinal motoneurons.<sup>11</sup> However, the cortex does not act alone, but it rather interacts with subcortical structures that are critical for flexible, dexterous actions.<sup>6,7,11,14–16</sup>

The striatum (STR) is a subcortical forebrain nucleus<sup>17</sup> that receives convergent input from MOp, secondary, parietal, and frontal cortical areas and projects to downstream nuclei of the basal ganglia.<sup>17–19</sup> The dorsal striatum (dSTR) is known to be critical for the establishment of motor skills guided by reinforcement teaching signals conveyed via dense innervation from midbrain dopamine neurons.<sup>6,14–17,20–23</sup> In analogy to the discrete action spaces of canonical reinforcement learning (RL)



models,<sup>24–27</sup> dSTR has long been proposed to play a specific and circumscribed role in action selection.<sup>14,20,23,28–33</sup> As a result, much of the experimental work on the basal ganglia has focused on analyzing the moments leading up to the initiation of a clearly identifiable action (e.g., move left or right<sup>26,27,32,34</sup>). However, since the very earliest dSTR recordings, it has also been noticed that modulation of activity is primarily during the execution of movements and more akin to the general pattern of activity in MOp.<sup>6,35–37</sup>

Two specific limitations in prior work have made it difficult to resolve the function of dSTR in action selection and specification of execution. First, there has been little work recording dSTR simultaneously with premotor and primary motor areas during execution of flexible and dexterous movements. Second, prior behavioral paradigms in rodents have often focused either on a single stereotyped action<sup>38</sup> or continuously varying actions,<sup>39,40</sup> without a requirement for both discrete selection of movements and continuous specification of execution parameters. In the current study, we address both of these limitations.

### Distinguishing predictions

In developing the behavioral paradigm used here, let us first clarify a key point: in the case of highly distinct actions, selection and specification hypotheses make essentially indistinguishable predictions about neural activity.<sup>6</sup> Take for example a comparison of activity between orienting left and right or a comparison of activity between rearing and locomotion.<sup>41,42</sup> According to a hypothesis in which dSTR is critical for action selection, these actions are associated with distinct active ensembles of neurons exclusively in dSTR<sup>32</sup>; note that some variants of this hypothesis do not require distinct ensembles found only in dSTR.<sup>43</sup> A hypothesis in which dSTR contributes to specification of execution can make the same prediction—different sets of muscles are being controlled with distinct spatiotemporal dynamics—which putatively requires distinct patterns of active neural populations.<sup>6,44,45</sup> This could lead one to suggest that the differences between specification and selection models are therefore merely “semantic” (i.e., not significantly different). While comparing two actions with very distinct parameters is a specific (limited) case in which the models can make the same prediction, here, we argue that selection and specification models make very distinct predictions when comparing neural activity across actions differing modestly in their execution parameters (Figures 1 and S1).

## RESULTS

Hypotheses in which dSTR participates in specification or selection make distinct predictions because they imply mechanistically distinct contributions to the control of movement that are reflected as either continuous, metric (specification), or discrete, non-metric (selection) neural correlates of action parameters. To see why this is the case, consider a common task—reaching to one of two possible targets that are far from each other—and two paradigmatic models: (1) a selection model in which discrete actions are reflected in non-overlapping neural ensembles and (2) a specification model with continuous parameterization of action

in the neural population activity (Figures 1 and S1). It is useful to visualize the projection of neuronal population activity onto dimensions that capture the majority of variance (principal components [PCs]) to reveal differences in these distinct model formulations. For very distinct actions (reaching to targets separated by 180°), population activity trajectories are well separated under either model (Figures 1 and S1). Contrast this with trajectories for two actions differing by only, say ~18°. A discrete selection model is powerful because it predicts distinct neural populations corresponding to each action regardless of how similar the kinematics are—thereby allowing reliable mapping of the selected action onto largely independent neural ensembles (i.e., Figure 5 in Klaus et al.<sup>32</sup> indicates that active ensembles must be less correlated than the ensembles in the input). In many accounts, the representations proposed are only static patterns associated with an action (e.g., Alexander et al.<sup>14</sup> and Klaus et al.<sup>32</sup>); however, this is clearly inconsistent with the complex temporal dynamics of dSTR (and MOp) activity during movement.<sup>38,39,46</sup> Thus, to “steelman” the selection model, we entertain a stronger version including a nearly orthogonal pattern that can evolve over time.<sup>6</sup> Under a specification model, however, the difference in population activity between similar actions is small. When neuron populations are tuned to the range for a continuous parameter of an action (e.g., cosine tuning to direction<sup>47</sup>), a small change in movement direction accounts for little variance. As a result, the leading PCs will now be dominated by the shared temporal dynamics of activity common across conditions,<sup>48,49</sup> and the trajectories of the leading PCs will exhibit small differences. Thus, a behavioral paradigm in which an animal is reliably selecting between actions with small parameter variation is uniquely useful for disambiguating the expected neural correlates between continuous (specification) or discrete (selection) action representations.

### Behavioral paradigm and neural recordings

To achieve this goal, we engineered a new joystick apparatus for head-fixed mice (Figure 2A).<sup>50,51</sup> The joystick was robotically positioned at one of two equidistant yaw angles (+5°/−15°; ~20 mm radially from hand rest) and independently commanded to force set points of 3 and 12 g (see STAR Methods). The mouse was required to reach out to the correct yaw target location, grab the joystick, and pull with sufficient force along the pitch axis to displace the joystick past a distance threshold (5 mm). All mice were trained to use the right forelimb, and all neural recordings were taken from the contralateral (left) hemisphere. Trials were divided into blocks dissociating joystick yaw location and/or pitch force requirements. In each session, mice completed 8 blocks, 2 repetitions of each of the 4 conditions (Figures 2A and 2B; location +5°/−15°, force set point 3/12 g, Video S1). On average, mice required 24 sessions to meet the training criterion, defined as the first complete execution of all 8 blocks (Figure 2E). Analysis of reach-to-pull behavior indeed revealed a double dissociation in reach trajectory angle across joystick location and applied pull force (Figures 2B, 2F, and 2G; repeated-measures ANOVA; reach angle,  $F_{3,12} = 135.7$ ,  $p = 8.25 \times 10^{-8}$ ; pull force,  $F_{3,12} = 57.93$ ,  $p = 3.30 \times 10^{-6}$ ) while maintaining levels of performance (>80% of trials successfully completed) comparable to reach-to-grasp tasks with a single

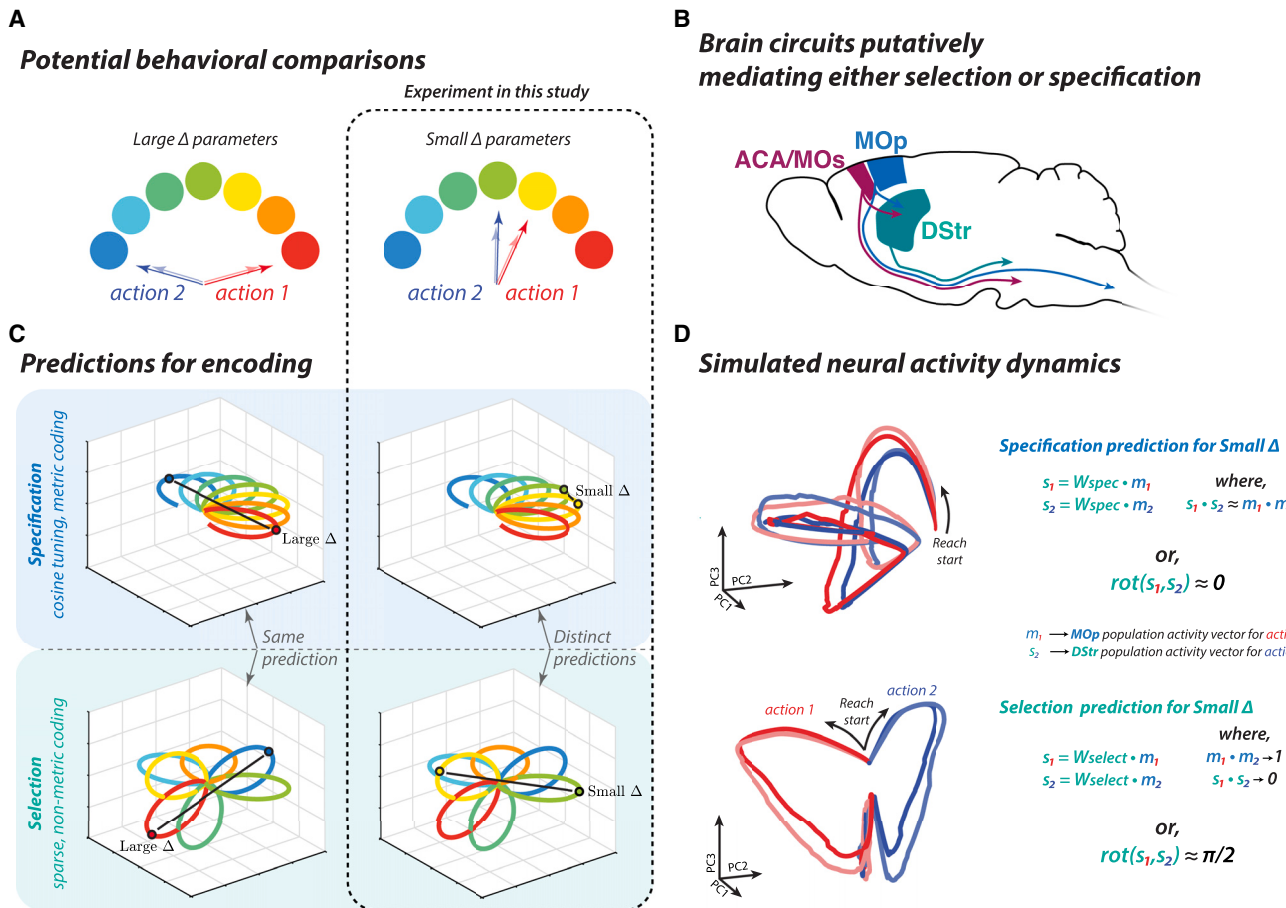


**Figure 1. Distinguishing predictions for neural activity under specification or selection models**

(A) There are different behavioral comparisons that can be made when trying to understand the neural representation of distinct actions: i.e., two actions with either large or small differences in parameterizations.

(B) Schematic of key brain areas studied.

(C) Predictions for the neural representation of actions in the case of a specification (upper row) or selection (lower row) model (color as in A). In the case of a specification model, neural activity encodes a metric space corresponding to different action parameters (e.g., cosine tuning on a flat manifold in neural space). The power of a selection mechanism is that activity is projected in separate directions for any given action in the space. For very distinct actions (left), these two models make indistinguishable predictions. However, for similar actions, the models make distinguishable predictions (right).

(D) Analysis of neural dynamics from simulated encoding models provides quantitative predictions for a selection model (lower) or specification model (upper). Simulated activity was projected onto the first three PCs. Right, quantitative description of a key difference (rotation angle between neural trajectories) for predictions of selection and specification hypotheses. See text and Figure S1 for further details.

target location.<sup>51–54</sup> One potential strategy to reach two lateralized targets involves systematically adjusting the initial hand positions based on the target locations. We confirmed that mice did not use this strategy (Figures 2C and 2D; *t* test; initial lateral position:  $t_{915} = 1.51$ ,  $p = 0.13$ ; initial outward position:  $t_{915} = 0.77$ ,  $p = 0.44$ ). Importantly, after training, performance did not differ systematically across trial types or between individual mice (Figure 2H; repeated-measures ANOVA,  $F_{3,12} = 1.33$ ,  $p = 0.32$ ).

#### Inactivation of corticostriatal projection impairs reach-to-pull

As noted above, the dSTR receives input from both MOp and frontal premotor areas.<sup>18,19,55,56</sup> To confirm that both sources of corticostriatal input are critical for performance of this task,

we examined how silencing primary motor (MOp → dSTR) or secondary motor/anterior cingulate (MOs/ACA → dSTR) projection neurons affected task performance. For optical silencing of projection neuron populations, we used intrastratial injection of rAAV2-retro into a dorsal striatal area known to retrogradely label both MOp and ACA in mice<sup>18,57</sup> (Figure 3A). We utilized a potent anion-conducting channelrhodopsin (soma-targeted GtACR2), previously demonstrated to robustly inactivate cortical projection neurons,<sup>51</sup> including corticostriatal neurons.<sup>58</sup> In randomly selected trials ( $p = 0.25$ ), the 473-nm bilateral silencing laser was triggered during the inter-trial interval and terminated either by a trial completion or after 4 s (Figure 3B). To control for visual perception of laser activation, stimuli were masked with ambient blue light.<sup>54</sup> We compared

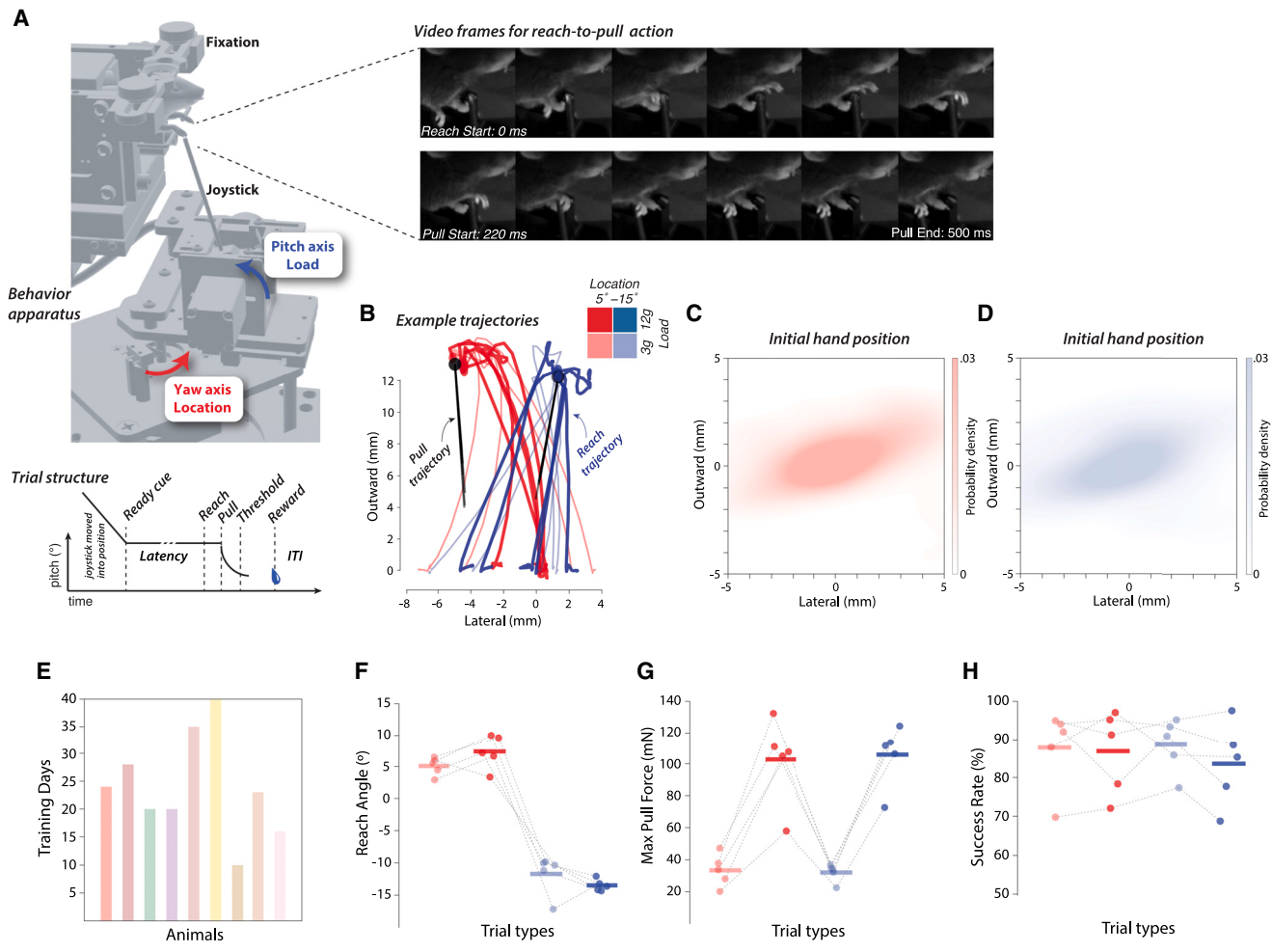


**Figure 2. Reach-to-pull task and analysis design to distinguish predictions of specification and selection functional accounts**

- (A) 3D rendering of robotic joystick apparatus indicating the key degrees of freedom and motorized control of pitch and yaw axes. Right, images from dual high speed camera video (Video S1). Lower, timeline for individual trials.
- (B) Example trajectories of successful reaches to each target (red and blue lines) and corresponding pulls (black lines). Trials comprise 4 types that vary in pull force (color intensity) and reach target location (blue vs. red). The lateral and outward coordinates are relative to the median initial hand position.
- (C and D) 2D kernel density estimates visualizing the distribution of initial hand positions for 5° (C) and -15° (D) target locations. The distributions were computed and plotted across a fixed spatial grid of -5 to 5 mm both laterally and outwardly.
- (E) The number of training sessions required for all nine mice to meet the training criterion.
- (F) Observed reach angle averaged across trials within all four combinations of pull force and reach target conditions. From the 9 trained mice, we collected both behavioral and neural data from 5 of them. For each mouse, we collected behavioral data from 1 to 4 sessions. Data across multiple sessions were averaged as one data point per animal ( $N = 5$ ). Horizontal bars represent the mean across animals.
- (G) Average observed pull force for each trial type.
- (H) Average success rate for each trial type.

the probabilities of successful reach start within 1 s after the joystick positioning (trial start). Suppression of activity in corticostriatal projections from both MOp and MOs/ACA led to a significant decrease in the probability of successful reach start (Figures 3E–3G; Wilcoxon signed-rank test; MOp:  $p = 0.03$ ; MOs:  $p = 0.004$ ). This is consistent with a key role for frontal cortical areas in movement initiation.<sup>8</sup>

Despite a significant reduction in the probability of reaching, mice still managed to execute a small number of successful reach-to-pull trials during optogenetic silencing (Figure 3E).

The initial hand positions in breakthrough trials were not distinguishable from those in control trials (Figures 3H and 3I; t tests; initial lateral position:  $t_{1,030} = 0.78$ ,  $p = 0.44$ ; initial outward position:  $t_{1,030} = 0.48$ ,  $p = 0.63$ ). Additionally, the initial hand positioning in breakthrough trials showed no bias relative to the target location (Figures 3H and 3I; t test; initial lateral position:  $t_{113} = 1.28$ ,  $p = 0.2$ ; initial outward position:  $t_{113} = 0.46$ ,  $p = 0.65$ ). However, we observed a modest but significant constriction of reach angles, indicating that reaching targets during corticostriatal inactivation were less separated relative to control

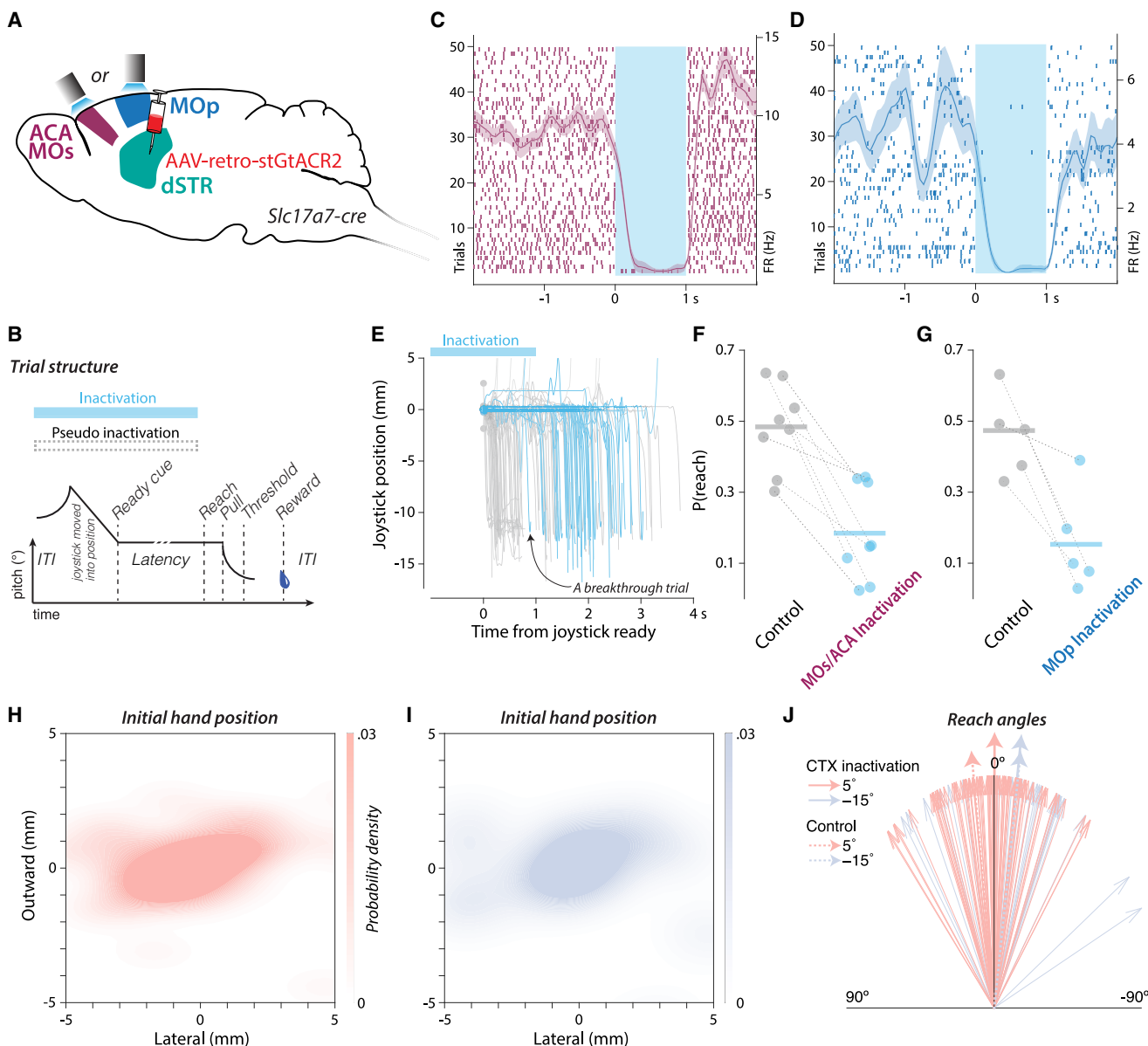


**Figure 3. Impact of corticostriatal neuronal inactivation on reach-to-pull performance and corresponding neural population trajectories**

(A) To selectively inactivate ACA/MOs or MOp neurons projecting to the dSTR, GtACR2 was expressed using rAAV2-retro injected into *Slc17a7-Cre* mice. (B) During corticostriatal inactivation sessions, ~25% of the total trials were randomly chosen to receive a 473-nm laser illumination targeted at ACA/MOs or MOp regions. In these trials, the laser activation occurred  $-2.74 \pm 1.2$  s (median  $\pm$  STD) before the joystick placement at the target location. The laser illumination lasted for up to 4 s and was discontinued if the mice successfully completed the trial or made an error.

(C and D) After session, neuronal silencing was validated by delivering fifty 1-s laser illuminations; two example neurons shown (C: MOs/ACA neuron; D: MOp neuron; blue area indicates time of illumination).

(E) Inactivation of MOs/ACA or MOp significantly reduced reach-to-pull occurrences as exemplified by joystick trajectories with (blue) or without (gray) the optical silencing.

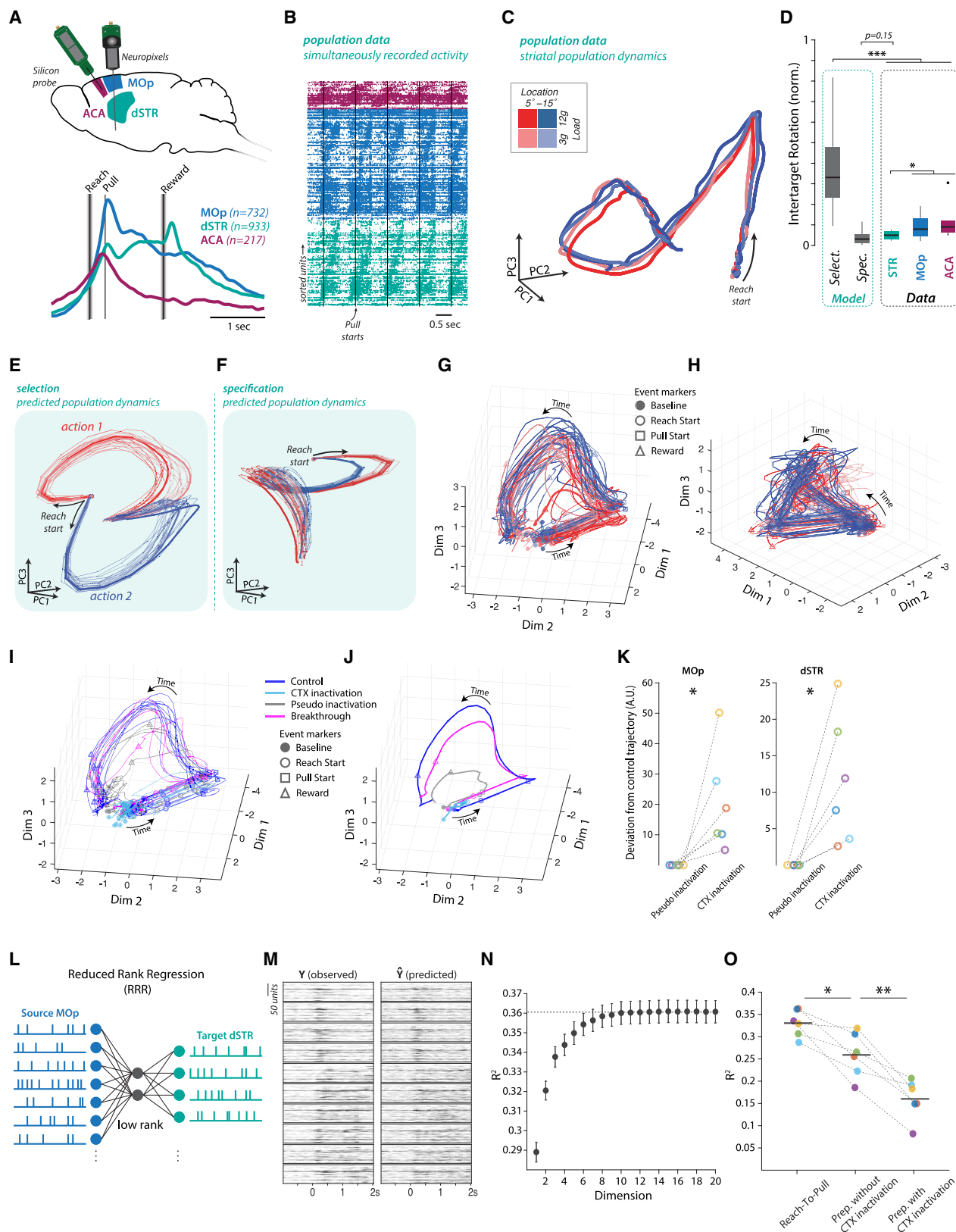
(F and G) Significant reduction in P(Reach) was observed during inactivation of MOs/ACA (F, 8 sessions from 4 mice) or MOp (G, 5 sessions from 4 mice).

(H and I) Visualizing kernel density estimates of initial hand positions during breakthrough trials (~10%) to 5° (H) and -15° (I) target locations.

(J) Trial-by-trial median-subtracted reach angles, with the mean angles for the two target locations shown as thicker solid arrows. Shorter dotted arrows are mean reach angles for control trials.

conditions (Figures 3J and S4I; t test on absolute-valued reach angles;  $t_{1,063} = 2.51$ ,  $p = 0.012$ ). Thus, corticostriatal activity appears to be critical for shaping continuous kinematics that guide

reaches to distinct targets. No other differences in parameters of breakthrough movements were found relative to control trials (Figures S4I–S4N).



(legend on next page)

### Neocortical and striatal activities exhibit complex temporal dynamics during movement execution

To measure neural activity in the forebrain, we acutely implanted a 384-channel Neuropixels probe targeting the forelimb motor cortex and the underlying dorsal to ventral STR (Figures 4A and 4B).<sup>51</sup> In addition, in several experiments, we also implanted a 64-channel silicon probe in the MOs/ACA, which is important for movement initiation and provides dense input to dSTR in areas also innervated by primary motor cortical areas.<sup>18,19,56,59</sup> From 5 mice, we recorded 732 (avg: 81.3, SD: 44.1) forelimb MOp, 933 (avg: 103.7, SD: 23.1; dorsal: avg: 69.9, SD: 24.5) STR units over 9 recording sessions. In addition, 217 (avg: 31.0, SD: 11.7) secondary motor and cingulate (MOs/ACA) units were recorded from 4 mice over 7 sessions (Figures 4A and 4B).

Both cortical and subcortical areas exhibited strong modulation throughout the reach-to-pull movement sequence and around the time of reward delivery (Figures 4A, 4B, S2, and S3). An example set of 5 sequential trials with raw spike rasters from ~350 units recorded simultaneously from MOs/ACA, MOp, and dSTR revealed highly reliable activity across repetitions of the reach-to-pull action (Figure 4B). It is clear even from this raw data across multiple trials that there are highly structured temporal dynamics of activity in both cortex and subcortical dSTR, consistent with previous descriptions in other forelimb operant tasks.<sup>6,36,38,39</sup> Next, we projected striatal activity onto the leading PCs derived from all recorded units, segregating the data by the four trial conditions (Figure 4C). We observed largely aligned activity trajectories that were dominated by the temporal dynamics of activity during reach-to-pull movements, which did not differ from the predictions of the specification model ( $p \sim 0.15$ , rank-sum test) but were outside the distribution of predictions from the selection model ( $p \ll 0.0001$ , rank-sum test; Figure 4D). Similarly, activity in MOp and MOs/ACA exhibited slightly greater rotations of population

activity across movements to the two targets, as compared with dSTR ( $p < 0.05$ , rank-sum test), even though we know that MOp in particular should not be (and is not) consistent with a selection model (Figure 1D).

We used Gaussian process factor analysis (GPFA<sup>60</sup>) to confirm that our comparison between the model and data is not sensitive to a specific dimensionality reduction method. First, projection of simulated encoding model data onto the top three axes identified by GPFA corroborated similar quantitative predictions of the selection model (Figure 4E) or the specification model (Figure 4F) as principal-component analysis (PCA) (Figure 1D). Consistent with the prediction of the specification model, shared temporal dynamics largely dominated neural population trajectories across the four trial conditions in both MOp and dSTR (Figures 4G and 4H). The reaching and pulling portions of the trajectories occupied largely orthogonal dimensions within the state space, reflecting the distinct neural dynamics for subcomponents of movement execution.

Using single-trial GPFA neural trajectories, we examined the impact of corticostriatal inactivation on cortical and striatal neural population activity. In contrast to the neural trajectories of successful reach-to-pull trials (Figures 4I and 4J; dark blue), those aligned to the onset of corticostriatal inactivation (Figures 4I and 4J; light blue) lacked the movement-related dynamics observed in control trials. However, breakthrough trials showed neural trajectories similar to control trials, despite substantial perturbation (Figures 4I, 4J, and S4; purple). The deviation of inactivation trajectories from the mean control trajectory was significantly greater than that of pseudo-inactivation trajectories in both MOp and dSTR neural populations (Figure 4K;  $t$  tests; MOp:  $t_5 = 3.01$ ,  $p = 0.03$ , dSTR:  $t_5 = 3.21$ ,  $p = 0.024$ ). These modest changes in low-dimensional dynamics and mean activity on breakthrough reach-to-pull actions belied a large change in the underlying pattern of activity in both cortex

**Figure 4. Electrophysiological recording of the cortical and striatal neural populations and their interactions during reach-to-pull performance**

- (A) Schematic of recording configurations used. Lower, mean perievent time histograms (PETHs) of mean activity aligned to the reach initiation in each major area targeted.
- (B) Raster plots of 5 sequential, concatenated trials for simultaneously recorded single units. Units are sorted according to time of peak activation.
- (C) Dynamics of striatal population activity for all sessions/trial types projected onto the first three PCs.
- (D) Normalized intertarget rotation in low-dimensional population activity trajectories for models (left) and data (right). Statistical significance was evaluated using multiple comparison corrections.
- (E and F) Analysis of simulated encoding models using GPFA corroborated quantitative predictions from the selection model (E) or the specification model (F) formulation, similar to those using PCA (Figures 1 and S1).
- (G and H) Representative single-trial neural trajectories plotted along the top three axes identified by GPFA. Ten trajectories (3 s long aligned to reach start) per trial type are plotted for simultaneously recorded MOp.
- (I) and (J) dSTR (H) populations and their means (thick lines). Key time points are marked on each trajectory.
- (I) Representative single-trial neural trajectories computed with GPFA. The trajectories of control and breakthrough trials are aligned to reach start, while those of inactivation and pseudo-inactivation are aligned to the onset of inactivation or a corresponding time point in the pseudo-inactivation trials.
- (K) Mean neural trajectories of each experimental condition.
- (L) Deviation from the mean control trajectory (Euclidean distance). Deviation of inactivation trials is normalized by subtracting distance of pseudo-inactivation trials.
- (M) Ten example striatal neural population activity (left) and the corresponding predictions by the RRR model (right).
- (N) Low-dimensional subspaces achieved equivalent predictability of the RRR model using the full dimensionality (marked with the dotted line).
- (O) Cortical inactivation significantly reduced the corticostriatal predictability (right) when applying the same model trained on neural activity during the reach-to-pull epoch (left). This reduction in predictability remained statistically significant even when compared with temporally matching epochs where no movement had occurred yet (preparatory epoch, center). \* $p < 0.05$ , \*\* $p < 0.01$ , \*\*\* $p < 0.001$ . For all analyses, data from 6 sessions collected across 4 mice were used.

(MOp/s) and dSTR (Figure S4). This further suggests that low-dimensional features of neural activity are critical for specification of movement kinematics and are at least partially degenerate with respect to the precise high-dimensional pattern of activity.<sup>12,61,62</sup> We note that degeneracy is a property of a model in which specification is a consequence of the conjoint pattern of activity across cortex and STR.

Descending corticostriatal projections suggest that striatal population activity should be partially predicted by observations of cortical activity. To test this, we utilized a reduced rank regression (RRR) model (see STAR Methods).<sup>63</sup> RRR is a dimensionality reduction method based on linear regression, which identifies the “communication subspace,” in which the activity of the source region predictive of the target region (MOp → dSTR, MOs/ACA → dSTR) is captured within low-dimensional subspaces (Figure 4L). Cross-validated predictions made by RRR closely matched the observed striatal activity in held-out trials, underscoring the significant influence of corticostriatal inputs on striatal dynamics (Figure 4M). Consistent with prior observations on interareal interactions,<sup>63,64</sup> corticostriatal communication also appears to be mediated through a low-dimensional subspace (Figure 4N). We observed the greatest explanatory power during movement execution (Figure 4O). Moreover, we found that corticostriatal predictability significantly decreased during corticostriatal neuron inactivation (Figure 4O).

### Cortex and subcortex jointly specify movement parameters

Despite the fact that mice reliably select between closely related actions differing in their direction and force parameters, we found little evidence for highly distinct neural ensembles in dSTR across conditions. Rather, the neural ensembles were substantially overlapping and were dominated by the complex temporal dynamics of activity during action execution (Figures 4A–4H, S2, and S3). However, there can still be dimensions in which population activity does differ according to reach-to-pull parameters. In the case of the specification model articulated above, these differences are not the primary source of variance, but they can be readily revealed using contrastive PCs (“cPCs”; see STAR Methods<sup>65</sup>; Figures 5A and S5). We first examined simulated activity from our action specification encoding model to confirm that activity projected onto cPCs reveals trial-type-specific geometry of activity that is not apparent in leading dimensions of standard PCA (Figure 5A, right). Consistent with predictions from the model, projecting population activity on cPCs revealed a distinct geometry of activity across reach-to-pull actions across target locations (Figure 5A) and pull force conditions (Figure S5). We also confirmed these results using demixed PCA (dPCA)<sup>66</sup> (Figure S5).

While this argues broadly in favor of dSTR involvement in action specification, there is still a substantial diversity of accounts within this broad class that we sought to further refine. For instance, a recent proposal<sup>16</sup> suggests a potential reconciliation of these findings: the dSTR may be responsible for selecting a “gross” action (i.e., reach-to-pull), while MOp determines fine specification of movement parameters (i.e., reach angle, pull force). We note that this would be surprising given that striatal activity is strongly correlated with continuous movement kine-

matics (Figures 5D, 5E, and S6),<sup>51,67,68</sup> necessary for specification of movement parameters,<sup>39,69,70</sup> and is sufficient to determine continuous kinematics.<sup>38,68</sup> Nonetheless, previous observations were made in tasks with single, highly stereotyped actions or highly variable movements rather than discrete selection between reach directions and pull forces studied here.

A model in which subcortical dSTR activity only defines the gross action whereas the motor cortex specifies fine parameters<sup>16</sup> makes several testable predictions. First, such a conceptualization implies that the dimensionality of population activity<sup>71</sup> should be lower in dSTR (one reach-to-pull action selected in all trials) when compared with MOp (four distinct reach-to-pull parameterizations specified). In contrast, if STR specifies movement parameters, then the dimensionality should be the same or greater as compared with motor cortical activity. We found that striatal activity exhibited a greater linear dimensionality than activity in MOp during the reach-to-pull task (Figure 5B<sup>72</sup>).

Second, if it is the case that dSTR activity only determines the gross action, then our ability to classify trial type from dSTR population activity should be worse than from MOp activity (implied by Figure 5A in Klaus et al.<sup>32</sup>, Figure 6 in Arber and Costa<sup>16</sup>). We trained decision-tree-based non-linear (random forest) classifiers to predict the trial type based on the activity of MOp, dSTR, and MOs/ACA activity during movement execution (see STAR Methods). Trial types could be classified with accuracy much higher than the chance level (25%) from all populations. We found no significant difference in the classification of trial types between MOp and dSTR populations across all datasets, disconfirming a prediction of a gross selection model (Figure 5C). Importantly, this classification performance is not ubiquitous. Classification based on activity in MOs/ACA, a premotor area critical to performance of this task, was significantly worse (Figure 5C; one-way ANOVA;  $F_{2,18} = 5.44, p = 0.014$ ).

Third, a model in which dSTR only selects gross action identity further implies that decoding of continuous movement kinematics from dSTR activity should be worse as compared with MOp. To address this question, we developed continuous-time Kalman filter-based decoders to reconstruct forelimb kinematics (see STAR Methods). Decoding accuracy was compared between neuron number-matched MOp and dSTR populations; the combined MOp + dSTR population served as an approximate upper bound. Decoding accuracies did not significantly differ (Figures 5E and S6; one-way ANOVA; reach:  $F_{2,18} = 0.51, p = 0.61$ ; pull:  $F_{2,21} = 0.63, p = 0.54$ ). For the recording sessions with simultaneous recording of all three regions, we compared performance of MOp, dSTR, and MOs/ACA decoders. A significant main effect of the region was found (Figure 5E; one-way ANOVA; reach:  $F_{2,12} = 17.06, p = 0.0003$ ; pull:  $F_{2,12} = 34.49, p = 1.06 \times 10^{-5}$ ), and the multiple comparison test with Bonferroni correction revealed comparable decoding accuracy between the neuron number-matched MOp and dSTR populations ( $p > 0.9$ ), whereas a significantly lower accuracy was obtained from the MOs/ACA population ( $p < 0.0005$ ) despite MOs/ACA → STR activity being necessary for task performance (Figure 3F).

### Single-neuron action parameter encoding

The above analyses all support a model in which dSTR, like MOp, is critical for the specification of movement parameters,

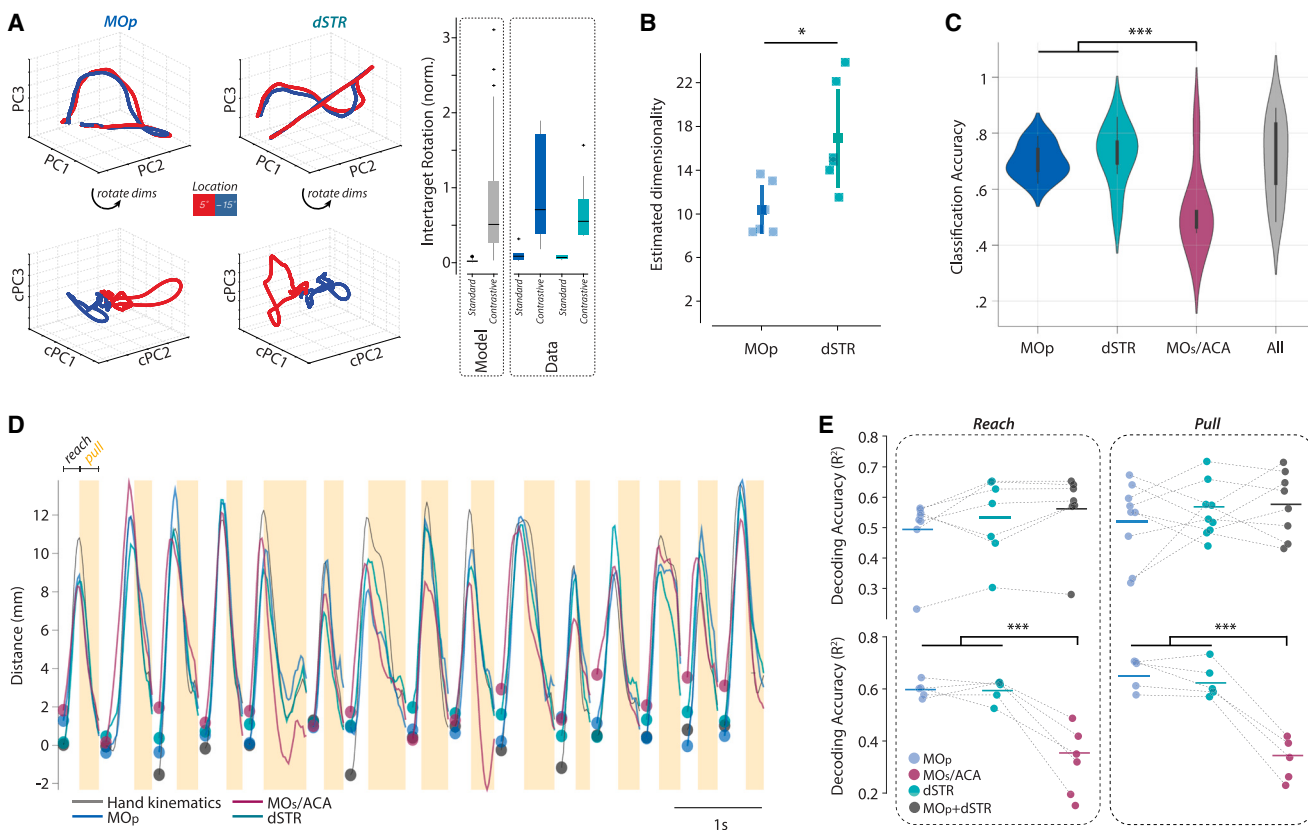


**Figure 5. Quantifying differences in the population encoding across trial conditions**

(A) Contrastive PCA (cPCA) was used to identify 3 components (cPC1–3) that maximally separate neural activity across target locations. Right, quantification of the rotation in population trajectories (analysis as in Figure 4D) predicted for an encoding model (left) compared with observed rotations in STR and MOp. There were no significant differences between model and data.

(B) Linear estimated dimensionality for the population of neurons recorded in each region. Each point is a separate dataset ( $N = 4$  mice;  $n = 6$  sessions).

(C) Random forest classifiers were used to classify the 4 trial types based on the peri-action neural activity with cross-validation and resampling to match the number of neurons across regions, i.e., same number of features (the number of neurons and time bins) was used for interregional comparison. To estimate an upper bound of the classifier performance, classifiers were trained using all simultaneously recorded neurons ("all").  $N = 5$  mice;  $n = 9$  sessions.

(D) The Kalman filter was used to decode 3D hand trajectories based on the peri-action neural activity with cross-validation and resampling to match the number of neurons across regions, based on our finding that the linear mapping between neural activity and limb states may differ in reach vs. pull phases. Thus, we trained separate decoders for reach and pull phases. For simplicity, trajectories on the y axis (outward) are displayed. See Figure S6 for detailed results.

(E) Accuracy of decoded trajectories was evaluated using the coefficient of determination ( $R^2$ ) separately for reach (left) and pull (right) phases, i.e., we quantified the variance in the actual hand trajectories explained by the decoded trajectories. Top, accuracy was compared between MOp and dSTR.  $N = 5$  mice;  $n = 9$  sessions. Bottom, accuracies of the three resampled brain regions were compared.  $N = 3$  mice;  $n = 5$  sessions.

yet the population-level analyses also suggest differences between the simultaneously recorded dSTR and MOp populations (e.g., linear dimensionality). In particular, one possibility is that dSTR exhibits preferential correlation for a subset of movement parameters. To look for such preferential encoding, we next examined the discriminability of individual neuronal activity as a function of reach direction and pull load with a measure of discriminability ( $d'$ ; see STAR Methods). Briefly,  $d'$  was computed by first taking the difference between the mean firing rate of each trial type and that of the remaining trials. The products of differential firing rates and vectors (2 targets  $\times$  2 forces) corresponding to each trial type were summed to yield  $d'$  scores across time within the 2D  $d'$  space. Individual units were classified into eight classes based on which trial types allowed for significant discrimination (examples shown in Figures 6A and S7).

Individual neurons in MOp distinguished both target location and pull load (Figures 6A and 6B). A neuron for which  $d'$  trajectory surpasses the 95% confidence interval of the trial-shuffled  $d'$  distribution (STAR Methods) was considered to encode a task variable(s) with statistical significance. Here, 67% of MOp neurons satisfied this criterion. Of these MOp neurons, a much greater fraction (47%) displayed directional tuning, while fewer neurons (9%) displayed load tuning (Figure 6B). Among the directionally tuned MOp neurons, a greater fraction (62%) was tuned for the contraversive (right) target (consistent with prior observations in primate MOp<sup>73</sup>). Interestingly, despite providing relatively poor decoding of trial-by-trial differences in movement kinematics, a similar fraction of individual neurons in MOs/ACA exhibited differential activity as a function of trial type (56%). In dSTR, we found that a substantial fraction of (61%) neurons

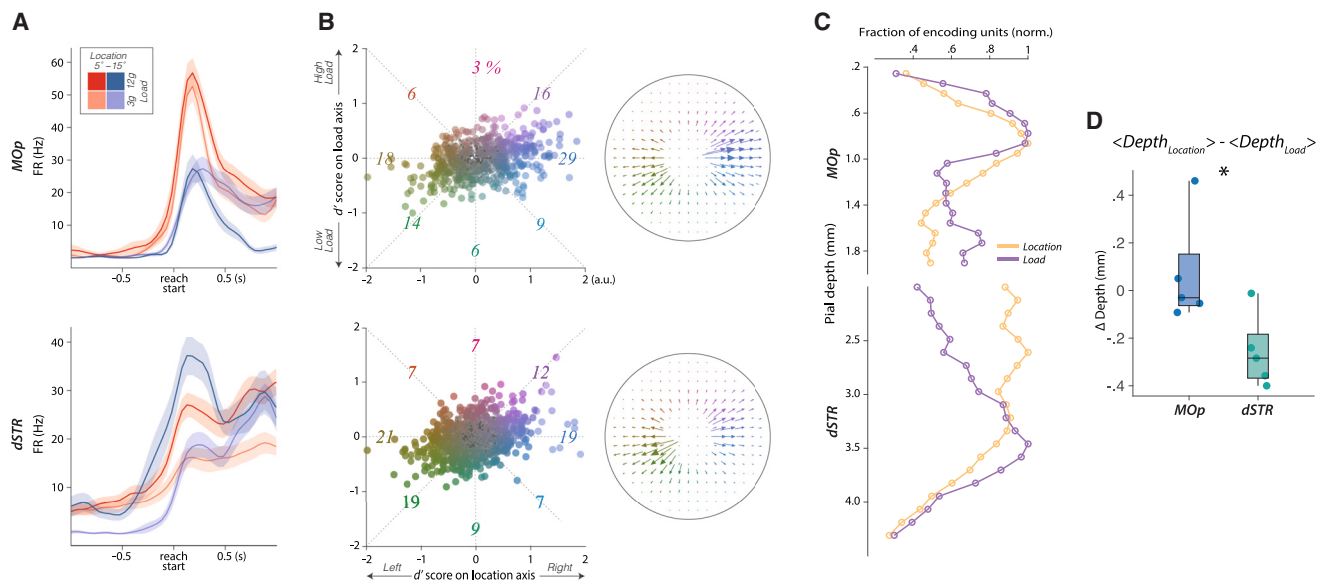


**Figure 6. Quantifying MOOp and dSTR single neuron encoding of trial conditions**

(A) Example individual neuron firing rates (top, MOOp unit; bottom, dSTR unit) aligned to reach start ( $t = 0$ ). Mean  $\pm$  SEM (shaded).

(B) Left, all MOOp (top) and dSTR (bottom) single units were distributed in a 2D encoding space comprising joystick location (horizontal) and load (vertical) axes (see STAR Methods). The 2D coordinates represent each unit's average distance from the origin during the 1-s period following the reach start. Units that passed a significance test based on each unit's trial-shuffled distribution were color coded according to their coordinates in the encoding space; non-significant units are marked as small gray circles. See Figure S7 for more example units. The color-coded numbers represent the percentage of encoding units classified into the 8 equidistant encoding groups. Right, quiver plots summarize the distribution of units within the encoding space. The counts were normalized across brain regions for inter-regional comparison and translated into the length of arrowed vectors.

(C) To compare the spatial distribution of encoding units across the corticostratal depths, the fraction of location- and load-encoding units were counted in depth bins and normalized to the maximum fraction across depths.

(D) The spatial segregation of dSTR units encoding the two movement parameters observed in (C) led to a significant difference in  $\Delta$  depths (difference in mean depths of the units that encode joystick location and load) between MOOp and dSTR ( $N = 5$  mice).

displayed tuning for the target location, joystick load, or both. Notably, a significantly greater fraction of STR neurons (16%) displayed sensitivity to the joystick load, compared with that of MOOp neurons (9%) (Figure 6B;  $\chi^2_1 = 7.61, p = 0.006$ ), while a greater fraction of MOOp neurons (47%) displayed sensitivity to target locations, compared with that of STR neurons (40%) (Figure 6B;  $\chi^2_1 = 5.0, p = 0.03$ ). This modest yet significant preferential encoding of the joystick load by individual STR neurons may be consistent with a critical role for STR, and basal ganglia broadly, in movement vigor.<sup>69,74,75</sup>

### Broad spatiotemporal distribution of movement parameter encoding in STR

Building upon anatomical evidence for topographic projections from cortex to STR,<sup>14,15,17</sup> many models propose that active neuronal ensembles for specific actions are restricted to tight spatial domains in STR.<sup>32</sup> At the same time, action parameter-specific correlates are distributed across corticostratal projection classes<sup>51</sup>; these classes have idiosyncratic and distributed anatomical projections to dSTR.<sup>56,76</sup> This suggests that action parameter-specific ensembles could be more spatially distributed in STR. To estimate these spatial distributions, we next examined individual neuronal  $d'$  as a function of anatomical location.

First, we examined the spatial distribution of types of neurons with significant  $d'$  scores for either joystick load or target location

parameters (Figure 6C; for “mixed” types, see Figure S7). In MOOp, we observed a relatively homogeneous distribution of types across the cortical layers; neurons with a significant  $d'$  concentrated in layer 5 (Figure 6C; Pearson correlation; all Rho values  $> 0.69$ ; all  $p$  values  $< 0.001$ ). Notably, a modest shift in depth was apparent, consistent with previous observations of preferential direction encoding in deep layer 5.<sup>51</sup> In contrast, we observed a more inhomogeneous spatial distribution in STR. We found that neurons with preferential target location correlates were densely populated dorsally, whereas neurons with preferential joystick load correlates were found in densest numbers more ventrally. Accordingly, the Pearson correlation of neuron fractions that encode target location and load was reduced (Pearson correlation; Rho = 0.41;  $p = 0.07$ ). While load- and location-encoding MOOp units were located at comparable depths, the pull force-encoding STR units were ventral to the reach direction-encoding units (Figure 6D; delta depths MOOp vs. dSTR; independent t test,  $t_8 = 2.68, p = 0.028$ ).

We next examined when during execution of the reach-to-pull action  $d'$  tended to peak for different trial types. In MOOp, normalized  $d'$  scores of these three encoding types displayed similar peri-action temporal patterns, as there was no significant interaction between time and encoding types (Figure S7J, top; repeated-measures ANOVA;  $F_{118,43837} = 0.95, p = 0.63$ ). In contrast, we observed a significant temporal segregation in

STR as the encoding of target location preceded the encoding of the joystick load (Figure S7J, bottom; repeated-measures ANOVA,  $F_{118,5336} = 2.24$ ,  $p = 3.03 \times 10^{-13}$ ). Thus, single neurons in STR provide similarly robust discrimination of movement parameters in roughly equal proportions to those in MOp; however, STR populations provide a less biased encoding that is also more distributed over space and time during reach-to-pull action.

### Cortex and STR conjointly specify movement parameters

The above analyses provide additional evidence that dSTR activity, like that of MOp, is sufficient to classify actions and carry information about continuous kinematics of reach-to-pull actions. We found little evidence that the dSTR was categorically biased toward a subset of movement parameters.<sup>10,16,35,37,44</sup> To quantitatively evaluate how trial-by-trial variations in observed MOp and STR activity account for variation in reach angle and pull force, we used a trial-based, linear committee decoder<sup>51</sup> that allows for a direct comparison to models, without having to consider continuous time dynamics of activity. Decoding performance using this approach was in general very good and could capture transitions around all switches in block conditions (Figure 7A). This is consistent with many lines of causal evidence that basal ganglia output and dSTR activity in particular determine continuous kinematics of movements.<sup>38,39,46,68,77,78</sup> However, we next sought to develop further analyses to strengthen this conclusion and more stringently evaluate a potential alternative. Namely, are these observed patterns of activity and decoding performance consistent with an alternative model in which dSTR activity is merely inherited from MOp but does not play a direct role in specifying the fine parameters of movement execution?

If two independent populations of units conjointly determine output, a decoder trained on both populations will correctly recover that each population contributes to the predicted output (Figure S8). Inspired by the organization of corticostriatal circuits,<sup>6</sup> we next consider a structure in which a population akin to MOp ("m") provides input to a downstream population akin to STR ("s"; via  $W_{m,s}$ ), and a weighted sum of the outputs of both populations determines the observed output ("O") akin to continuous variation in a movement parameter (Figure 7B; see STAR Methods for details).<sup>17–19</sup> At one extreme, when  $W_{m,s}$  is unstructured (random) and O is purely driven by m, the decoding is appropriately much better from m compared with s (Figure 7C; red point). At the other extreme, when  $W_{m,s}$  acts to pool and denoise m activity but O is determined by m only, then decoding can indeed indicate a greater contribution from s than m that is not present (Figure 7C; yellow point). Consistent with the interpretation that this is due to pooling and denoising, this effect is well predicted by an enhanced pairwise correlation of s activity (Figure 7C). There is little empirical support for a purely excitatory and focused topography with no lateral inhibition in corticostriatal connectivity,<sup>17–19,79</sup> and similarly, we observed reduced rather than elevated pairwise correlations in dSTR activity patterns (Figure S8; STR:  $0.17 \pm 0.02$  [SD]; MOp:  $0.19 \pm 0.03$ ). Distributed topographic connectivity combined with modest lateral inhibition, consistent with corticostriatal anatomy,<sup>17–19,79</sup>

was able to recapitulate both reduced pairwise correlations in s and decoding performance that reflected ground truth contribution to output (Figures 7D and 7E).

We quantitatively evaluated decoding performance in our datasets using the same decoding methodology. Across all recording sessions, we found similar, good performance of decoders trained on MOp and STR populations (Figure 7D). Plotting decoding performance in STR vs. MOp revealed a negatively sloped trade-off in good quantitative agreement with model predictions over a range of roughly equal contribution (Figure 7E). The data were skewed toward models in which MOp and STR make relatively balanced contributions. Specifically, we observe reliably better decoding from STR activity for both pull force ( $p = 0.008$ ; rank-sum test) and reach angle ( $p = 0.0005$ ; rank-sum test). The observed high decoding performance from STR and worse decoding from MOp when both areas are used jointly in decoding, are thus more consistent with predictions of a model in which the conjoint activity of MOp and STR determine movement parameters.

### Neocortical contribution to specification can decrease with experience

We found that the relative MOp/STR contribution to specifying movement parameters appeared to vary across subjects. Conjoint specification could allow partially separable circuits to modify the same action.<sup>7</sup> For example, rapid top-down explicit control (say following instruction<sup>2</sup>) could modify movement speed via direct modulation of MOp activity. Alternatively, experience with selective reinforcement for actions performed within a specific range of parameters<sup>68</sup> could implicitly modify movement via dopamine-dependent modulation of synaptic weights on STR neurons<sup>80</sup> without modifying MOp population activity. Recent work studying stereotyped forelimb movements found that MOp is only critical for acquisition and STR critical after initial learning.<sup>81,82</sup> This would suggest that when learning a new action parameterization MOp might be a greater contributor relative to STR,<sup>44</sup> and training history did differ across individual subjects in our dataset (Figure 2E). To examine this possibility, we trained a new pair of mice on a single target location and joystick load. We then recorded neural activity primarily in MOp during the very early exposure (<3 sessions prior) to a novel target location and/or joystick load requirement. To compare MOp decoding performance, we examined reconstruction error (root-mean-square error [RMSE]). We find that in these new mice experiencing a novel joystick load, decoding performance from MOp activity was better than observed in any of the 9 datasets examined in well-trained animals (Figure 8). Indeed, in well-trained mice, MOp decoding performance was significantly negatively correlated with the extent of training experience, and the new session data were consistent with that trend (Figure 8B). However, we found no such correlation for reach angle decoding, suggesting a sustained, critical role of MOp even with extensive training. Moreover, there was no significant correlation in our accuracy at decoding movement kinematics or kinetics from dSTR activity in trained animals ( $p = 0.43$ ), suggesting that dSTR contributions may be relatively constant after training, consistent with the persistent sensitivity of forelimb motor skills to dSTR inactivation.<sup>38,39</sup>

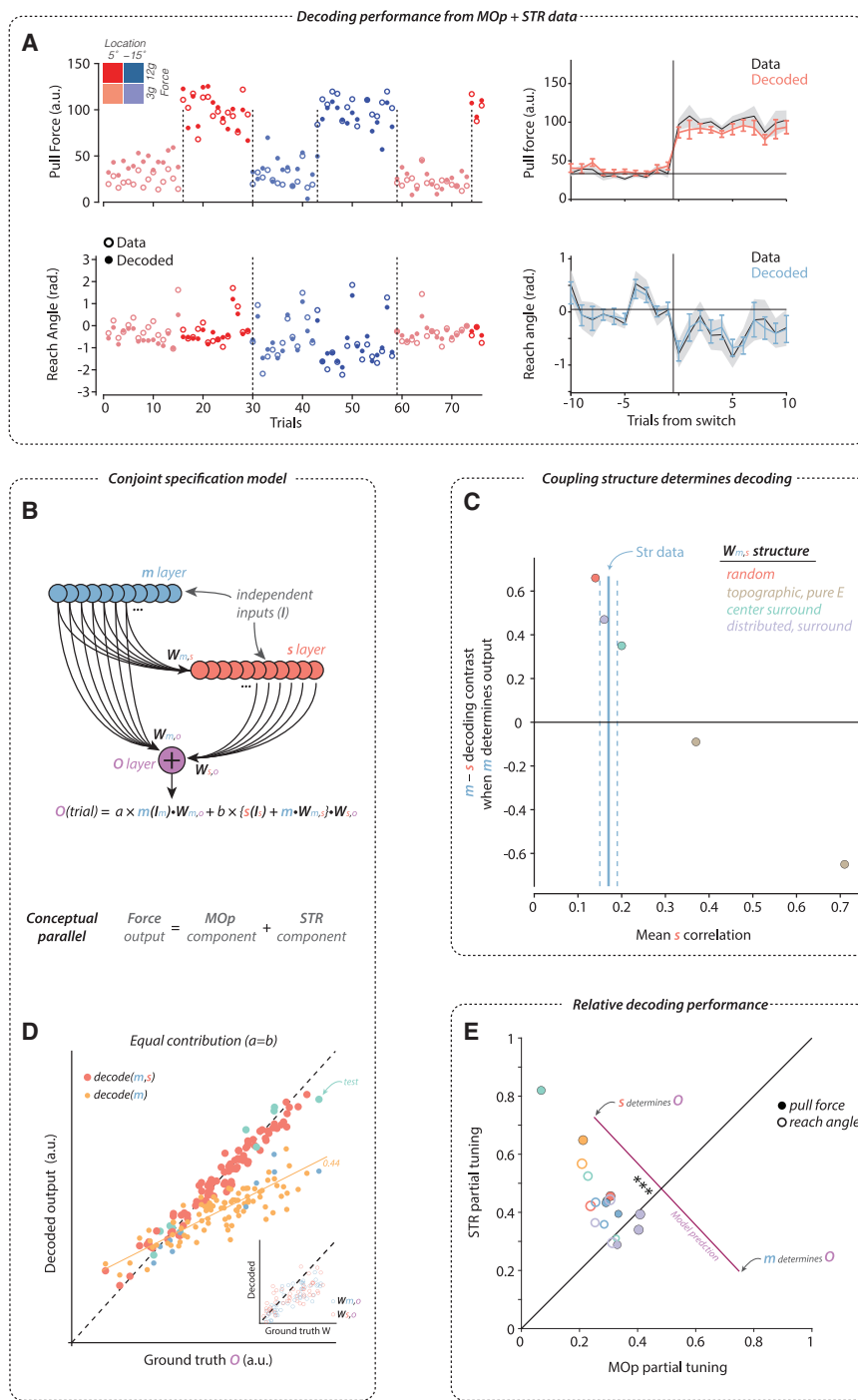


**Figure 7. A conjoint specification model can best explain relative decoding performance of MOp and STR**

(A) Observed (open circles) pull force (upper) and reach angle (lower) are plotted for each trial for 4 trial types (as indicated by color code). This was compared with predictions from a linear decoder (filled circles; see STAR Methods). Right plots indicate the mean and standard error (shaded) for data (black) and the mean and standard error (bars) for decoded (colored) around all up switches in pull force (upper) and all down switches in target angle (lower).

(B) Schematic for two populations of units connected as in corticostriatal connectivity.  $m$  layer (blue) corresponds to MOp, and  $s$  layer (red) corresponds to STR. The output,  $O$ , was modeled as a weighted sum of output from the  $m$  and  $s$  layers.

(C) The difference in decoder tuning derived from  $m$  or  $s$  populations is plotted as a function of the pairwise correlation of activity in the  $s$  population across trials for a model configuration in which only  $m$  determines  $O$ . Only decoders that recover positive values are accurately detecting model structure. Colors correspond to different formulations of  $W_{m,s}$  structure (see STAR Methods). Solid, vertical blue line is the mean pairwise correlation in STR data across all sessions (dashed lines indicate standard deviation).

(D) The same committee decoder performance as applied to encoding model data and plotted for decoded predictions (y axis) compared with observed ground truth output (x axis) for a decoded using the full  $m$  and  $s$  layer data (larger, redder circles) and partial decoding from just  $m$  layer activity (smaller, yellow circles). Inset, the inferred weights from the committee decoder are well correlated with the ground truth  $W$  (x axis). Light blue points are cross-validation test samples not used in training.

(E) Decoding of pull force (filled) and reach angle (open) from data from STR (y axis) is plotted against MOp (x axis) for all sessions. Purple line indicates the expected trade-off in decoder performance for models where either exclusively  $s$  or exclusively  $m$  determines  $O$ . Contribution from STR compared with MOp; sign-rank test; \*\*\* $p$  < 0.001.

## DISCUSSION

Canonical models invoke an abstracted representation of action in dSTR subserving selection<sup>16</sup> and initiation<sup>14,15</sup> of gross actions. This is in distinction to the continuous specification of movement kinematics and kinetics in online control of execution by MOp.<sup>5,11</sup> However, recent proposals highlight critical roles of dSTR in specifying the detailed movement parameters underlying

goal-directed actions<sup>6,37,38,44</sup> and have argued against a role primarily in action selection.<sup>68,77,83</sup> As we show using quantitative but simple models, most existing datasets are equivocal on this distinction (Figures 1 and S1). These models can be distinguished by recording MOp and STR activity as an animal chooses between the same gross action with modest variation in the parameters of the underlying movements. Here, we developed such a paradigm, and our data are uniquely consistent with a model in which the fine movement parameters underlying a reach-to-pull action are the product of conjoint specification by MOp and STR.<sup>6,37,84</sup> Our data are inconsistent with several

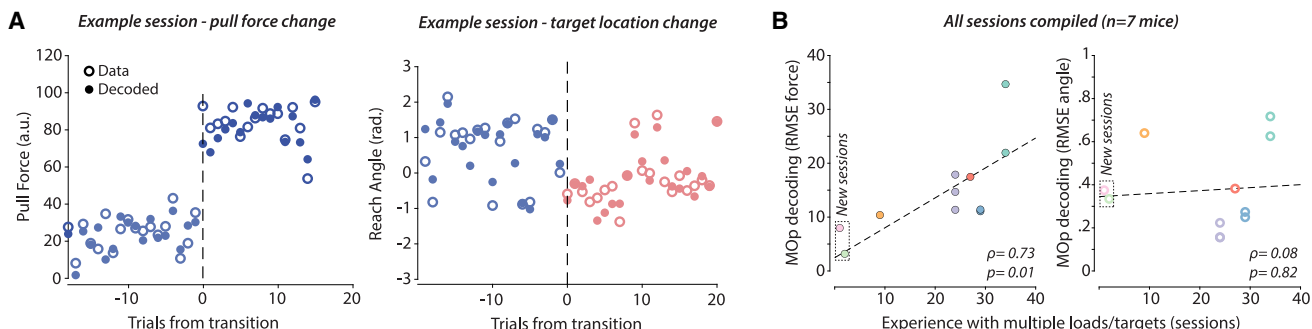


**Figure 8. Encoding of novel movement parameters may reflect MOp-driven specification of novel forces**

(A) Observed (open circles) pull force (left) and reach angle (right) are plotted around the transition to a new pull load and target location in an example session. Decoding from MOp population recording as in Figure 7.

(B) Quantification of the accuracy of MOp-alone decoder performance for applied force (left) and reach angle (right), plotted as a function of the total number of sessions of experience with multiple targets/loads. In addition to previous mice ( $N = 5$ ), two new mice were trained on a single joystick load and single location. We then computed the decoding performance on the first day as they transitioned to a novel load and target location ("new sessions"). Regression line is fit across all data ( $N = 7$  mice;  $n = 11$  sessions). Significant correlation was also detected in just the subset of trained mice ( $N = 5$ ;  $p < 0.05$ , not plotted) for force. Colors indicate individual mice.

predictions of a model in which dSTR selects gross actions.<sup>16,43,85</sup> It is worth noting, however, that this is not to say that animals do not select actions, *nor* that no other brain area is critical for action selection.

This work replicates and builds upon previous work that has described robust dSTR encoding of kinematics in the case of both highly variable<sup>39,40,51,67,68</sup> and stereotyped<sup>38,86</sup> actions. Calcium imaging data have, in some cases, suggested an absence of dSTR encoding of movement kinematics.<sup>41,42</sup> However, this may be a limitation inherent to calcium imaging in STR<sup>87,88</sup> or a result of failing to examine variation in relevant movement kinematics in detail,<sup>46</sup> as other imaging studies do find clear kinematic correlates.<sup>89,90</sup> In the cortex, where direct comparisons between electrophysiology and imaging have been made, continuous behavioral correlates can be harder to identify with calcium imaging.<sup>51,91</sup> We observed encoding of movement parameters to be distributed over millimeters of depth in STR, whereas imaging has typically explored only a very limited depth and thus may have missed dorsoventrally distributed correlates.<sup>50</sup> Finally, we show that activity in the putative premotor region in MOs/ACA—despite being critical for reach-to-pull actions—has significantly worse decoding of fine movement parameters. Thus, while non-negligible encoding of gross movement parameters may be ubiquitous,<sup>92,93</sup> fine parameter variation of an action can be preferentially decoded from specific forebrain regions.

How might conjoint specification of movement parameters by MOp and STR be useful for different aspects of learned, adaptive voluntary action? There are some data to suggest that subcortical basal ganglia activity dynamics are inherited from and redundant with cortical dynamics.<sup>94,95</sup> However, the observation of relatively normal kinematics despite substantially altered activity patterns in breakthrough trials provides direct evidence for a different interpretation: the neural specification of actions is degenerate with respect to the precise pattern of population activity in MOp/s and dSTR. What may seem redundant for one aspect of behavior (e.g., executing a well-learned action)

may afford unique opportunities for other aspects of behavior (e.g., differential learning mechanisms). Computational modeling with artificial neural networks demonstrates that distinct architectures can achieve equivalent output performance,<sup>72,96–99</sup> and this is an implication of "dynamical" models of motor control.<sup>12,61,62</sup> Consistent with this general insight, here, we observed similarly good decoding performance from either MOp or STR activity<sup>51</sup> yet greater spatiotemporal separation of individual neuron encoding in dSTR. STR receives dense innervation from MOs/ACA, partially overlapping and partially distinct from MOp innervation,<sup>18,19,22,57,100</sup> which may help to explain greater spatiotemporal distribution of movement variable encoding. MOs/ACA projections to STR appear critical for initiation of actions and exhibit the earliest pre-reach modulation of activity in mice (here) as described extensively in primates.<sup>8</sup> This is not unique to corticostriatal connectivity as thalamocortical connectivity is also critical for forelimb reach initiation.<sup>101–103</sup> MOs/ACA also projects densely to non-STR targets (e.g., zona incerta<sup>19,104</sup>) more weakly innervated by MOp. These extra-telencephalic projections may help to explain a critical role of MOs/ACA in the initiation of an action or could mediate processes thought to modulate initiation (e.g., "urgency"<sup>83</sup>) with correlates carried by MOs/ACA → STR collateral projections.<sup>105</sup>

There are many differences between afferent inputs to MOp and dSTR. For example, dSTR receives dense innervation from midbrain dopamine neurons, amygdala, and intralaminar thalamic areas that innervate MOp less. The involvement of basal ganglia<sup>20,27</sup> and amygdala<sup>106,107</sup> in RL has led to the proposal that the representations of movement parameters in dSTR are critical for slow learning of implicit movement specification.<sup>44,80</sup> More rapid learning, in some cases involving explicit specification of movement parameters,<sup>108</sup> is thought to be dependent on cortex.<sup>109</sup> Consistent with this possibility, we provide evidence across seven mice, including two mice learning a novel pull force, that lesser training extent is associated with an enhanced MOp contribution.<sup>82</sup> However, even in the well-trained condition, many lines of evidence indicate

that MOp and STR continue to play a conjoint role in specifying the movement parameters underlying skilled forelimb movements in mice and mammals generally.<sup>11,51,68,101,109</sup> The robustness to MOp lesion for some stereotyped (although not flexible<sup>6,86</sup>) forelimb actions may reflect a differential capacity to compensate for loss of MOp function that arises with training (requiring >1 week<sup>110–112</sup>), rather than necessarily implying a sequential, functional handoff (“tutoring”<sup>37,38</sup>) between cortical and subcortical areas.

There has been some progress articulating putative learning rules in MOp<sup>113</sup> and STR,<sup>68</sup> which might allow the flexible specification of fine parameters of goal-directed, skilled actions. However, many critical questions remain from the perspective of a conjoint specification model as proposed here. How are plastic changes across these cortical and subcortical circuit components coordinated?<sup>80</sup> How is specificity across multiple distinct learned actions maintained?<sup>64</sup> Does conjoint specification arise as a necessary transition during development to more slowly developing corticospinal control?<sup>7,114,115</sup> These and other questions will be critical to address in future studies.

## RESOURCE AVAILABILITY

### Lead contact

Requests for further information and/or resources should be directed to the lead contact, Joshua T. Dudman ([dudman@janelia.hhmi.org](mailto:dudman@janelia.hhmi.org)).

### Materials availability

All materials used in this study are available and described in the STAR Methods and/or our lab website <https://dudlab.notion.site/Conjoint-specification-of-action-in-neocortex-and-striatum-cebef9fc306947139f0ee70ce2dadeaa?pvs=4>.

### Data and code availability

All data and code used in the analysis will be made available on public databases as described in STAR Methods (code: GitHub; data: FigShare) and collected together at: <https://dudlab.notion.site/Conjoint-specification-of-action-in-neocortex-and-striatum-cebef9fc306947139f0ee70ce2dadeaa?pvs=4>.

Software FigShare: <https://doi.org/10.25378/janelia.28025357>.

Dataset FigShare: <https://doi.org/10.25378/janelia.28025282>.

Any additional information required to reanalyze the data reported in this paper is available from the lead contact upon request.

## ACKNOWLEDGMENTS

We thank all the members of the Dudman and Gallego labs for project feedback; J. Arnold, Janelia Experimental Technologies for designing the hardware for the joystick apparatus and P. Polidoro for designing the software control, both under extensive interaction and iteration with J. Park; J. Keller and S. Gong for providing technical assistance for hardware; the Janelia Viral Resources team for supplying reagents; and M. Copeland and B. Foster for assistance with histology. The analysis in Figure 8B was inspired by a helpful discussion with Emmett Thompson (SWC) and Francesca Greenstreet (SWC) at iBAGS 23. This work was supported by Howard Hughes Medical Institute where J.T.D. is a Senior Group Leader at the Janelia Research Campus.

## AUTHOR CONTRIBUTIONS

Conceptualization, J.T.D., J.P., P.P., and J.A.; methodology, J.P., P.P., J.A., J.A.G., and J.T.D.; investigation, J.P., C.F., J.T.D.; visualization, J.P., C.F., and J.T.D.; funding acquisition, J.T.D.; project administration, J.T.D.; supervision, J.T.D. and J.A.G.; writing—original draft, J.P. and J.T.D.; writing—review & editing, J.P., J.T.D., J.A.G., B.M., C.F., J.A., and P.P.

## DECLARATION OF INTERESTS

The authors declare no competing interests.

## STAR METHODS

Detailed methods are provided in the online version of this paper and include the following:

- **KEY RESOURCES TABLE**
- **EXPERIMENTAL MODEL AND STUDY PARTICIPANT DETAILS**
- **METHOD DETAILS**
  - A novel joystick apparatus
  - Training and performance in the Reach-to-Grasp task
  - Histology
- **QUANTIFICATION AND STATISTICAL ANALYSIS**
  - Extraction of 3-D hand and joystick trajectories using DeepLabCut
  - Extracellular electrophysiological recording
  - Gaussian Process Factor Analysis
  - Reduced Rank Regression
  - Dimensionality estimate
  - Principal Component Analysis and contrastive Principal Component Analysis
  - Neural decoding of 3D hand trajectories with Kalman filter
  - Random forest classifier
  - Characterization of individual neuronal encoding of trial types with d'
  - Committee decoder design
  - Encoding simulated data
  - Two population decoding simulated data

## SUPPLEMENTAL INFORMATION

Supplemental information can be found online at <https://doi.org/10.1016/j.neuron.2024.12.024>.

Received: September 27, 2023

Revised: September 9, 2024

Accepted: December 19, 2024

Published: January 20, 2025

## REFERENCES

1. Bernstein, N.A. (1967). *The Co-Ordination and Regulation of Movements* (Pergamon Press).
2. Wong, A.L., Haith, A.M., and Krakauer, J.W. (2015). Motor Planning. *Neuroscientist* 21, 385–398.
3. Andersen, R.A., and Cui, H. (2009). Intention, action planning, and decision making in parietal-frontal circuits. *Neuron* 63, 568–583.
4. Cisek, P., and Kalaska, J.F. (2010). Neural mechanisms for interacting with a world full of action choices. *Annu. Rev. Neurosci.* 33, 269–298.
5. Kalaska, J.F. (2009). *Progress in Motor Control* (Springer).
6. Park, J., Coddington, L.T., and Dudman, J.T. (2020). Basal Ganglia Circuits for Action Specification. *Annu. Rev. Neurosci.* 43, 485–507. <https://doi.org/10.1146/annurev-neuro-070918-050452>.
7. Gmaz, J.M., Keller, J.A., Dudman, J.T., and Gallego, J.A. (2024). Integrating across behaviors and timescales to understand the neural control of movement. *Curr. Opin. Neurobiol.* 85, 102843.
8. Picard, N., and Strick, P.L. (2001). Imaging the premotor areas. *Curr. Opin. Neurobiol.* 11, 663–672.
9. McFarland, N.R., and Haber, S.N. (2000). Convergent inputs from thalamic motor nuclei and frontal cortical areas to the dorsal striatum in the primate. *J. Neurosci.* 20, 3798–3813.
10. Shadmehr, R., and Krakauer, J.W. (2008). A computational neuro-anatomy for motor control. *Exp. Brain Res.* 185, 359–381.

11. Lemon, R.N. (2008). Descending pathways in motor control. *Annu. Rev. Neurosci.* 31, 195–218.
12. Shenoy, K.V., Sahani, M., and Churchland, M.M. (2013). Cortical control of arm movements: a dynamical systems perspective. *Annu. Rev. Neurosci.* 36, 337–359.
13. Scott, S.H. (2004). Optimal feedback control and the neural basis of volitional motor control. *Nat. Rev. Neurosci.* 5, 532–546.
14. Alexander, G.E., Crutcher, M.D., and DeLong, M.R. (1990). Basal ganglia-thalamocortical circuits: parallel substrates for motor, oculomotor, "prefrontal" and "limbic" functions. *Prog. Brain Res.* 85, 119–146.
15. Albin, R.L., Young, A.B., and Penney, J.B. (1989). The functional anatomy of basal ganglia disorders. *Trends Neurosci.* 12, 366–375.
16. Arber, S., and Costa, R.M. (2022). Networking brainstem and basal ganglia circuits for movement. *Nat. Rev. Neurosci.* 23, 342–360. <https://doi.org/10.1038/s41583-022-00581-w>.
17. Dudman, J.T., and Gerfen, C.R. (2015). The basal ganglia. *The Rat Nervous System*, Fourth Edition (Academic Press).
18. Pan, W.X., Mao, T., and Dudman, J.T. (2010). Inputs to the dorsal striatum of the mouse reflect the parallel circuit architecture of the forebrain. *Front. Neuroanat.* 4, 147.
19. Oh, S.W., Harris, J.A., Ng, L., Winslow, B., Cain, N., Mihalas, S., Wang, Q., Lau, C., Kuan, L., Henry, A.M., et al. (2014). A mesoscale connectome of the mouse brain. *Nature* 508, 207–214.
20. Doya, K. (2000). Complementary roles of basal ganglia and cerebellum in learning and motor control. *Curr. Opin. Neurobiol.* 10, 732–739.
21. Bar-Gad, I., Morris, G., and Bergman, H. (2003). Information processing, dimensionality reduction and reinforcement learning in the basal ganglia. *Prog. Neurobiol.* 71, 439–473.
22. Haber, S.N. (2003). The primate basal ganglia: parallel and integrative networks. *J. Chem. Neuroanat.* 26, 317–330.
23. Mink, J.W. (1996). The Basal Ganglia: Focused selection and inhibition of competing motor programs. *Prog. Neurobiol.* 50, 381–425.
24. Sutton, R.S., and Barto, A.G. (1998). Reinforcement Learning: An Introduction (MIT Press).
25. Daw, N.D., and Dayan, P. (2014). The algorithmic anatomy of model-based evaluation. *Philos. Trans. R. Soc. Lond. B Biol. Sci.* 369, 20130478. <https://doi.org/10.1098/rstb.2013.0478>.
26. Corrado, G., and Doya, K. (2007). Understanding neural coding through the model-based analysis of decision making. *J. Neurosci.* 27, 8178–8180.
27. Schultz, W. (2015). Neuronal Reward and Decision Signals: From Theories to Data. *Physiol. Rev.* 95, 853–951.
28. Deniau, J.M., Mailly, P., Maurice, N., and Champier, S. (2007). The pars reticulata of the substantia nigra: a window to basal ganglia output. *Prog. Brain Res.* 160, 151–172.
29. Graybiel, A.M. (1998). The basal ganglia and chunking of action repertoires. *Neurobiol. Learn. Mem.* 70, 119–136.
30. Aldridge, J.W., and Berridge, K.C. (1998). Coding of serial order by neostriatal neurons: a "natural action" approach to movement sequence. *J. Neurosci.* 18, 2777–2787.
31. Buchwald, N.A., Hull, C.D., and Levine, M.S. (1979). Basal ganglionic neuronal activity and behavioral set. *Appl. Neurophysiol.* 42, 109–112.
32. Klaus, A., Alves da Silva, J., and Costa, R.M. (2019). What, If, and When to Move: Basal Ganglia Circuits and Self-Paced Action Initiation. *Annu. Rev. Neurosci.* 42, 459–483.
33. Joel, D., Niv, Y., and Ruppin, E. (2002). Actor–critic models of the basal ganglia: new anatomical and computational perspectives. *Neural Netw.* 15, 535–547.
34. Inagaki, H.K., Chen, S., Daie, K., Finkelstein, A., Fontolan, L., Romani, S., and Svoboda, K. (2022). Neural Algorithms and Circuits for Motor Planning. *Annu. Rev. Neurosci.* 45, 249–271. <https://doi.org/10.1146/annurev-neuro-092021-121730>.
35. Yin, H.H. (2014). Action, time and the basal ganglia. *Philos. Trans. R. Soc. Lond. B Biol. Sci.* 369, 20120473.
36. Anderson, M.E., and Horak, F.B. (1985). Influence of the globus pallidus on arm movements in monkeys. III. Timing of movement-related information. *J. Neurophysiol.* 54, 433–448.
37. Turner, R.S., and Desmurget, M. (2010). Basal ganglia contributions to motor control: a vigorous tutor. *Curr. Opin. Neurobiol.* 20, 704–716.
38. Dhawale, A.K., Wolff, S.B.E., Ko, R., and Ölveczky, B.P. (2021). The basal ganglia control the detailed kinematics of learned motor skills. *Nat. Neurosci.* 24, 1256–1269.
39. Panigrahi, B., Martin, K.A., Li, Y., Graves, A.R., Vollmer, A., Olson, L., Mensh, B.D., Karpova, A.Y., and Dudman, J.T. (2015). Dopamine Is Required for the Neural Representation and Control of Movement Vigor. *Cell* 162, 1418–1430.
40. Kim, N., Barter, J.W., Sukharnikova, T., and Yin, H.H. (2014). Striatal firing rate reflects head movement velocity. *Eur. J. Neurosci.* 40, 3481–3490.
41. Markowitz, J.E., Gillis, W.F., Beron, C.C., Neufeld, S.Q., Robertson, K., Bhagat, N.D., Peterson, R.E., Peterson, E., Hyun, M., Linderman, S.W., et al. (2018). The Striatum Organizes 3D Behavior via Moment-to-Moment Action Selection. *Cell* 174, 44–58.e17. <https://doi.org/10.1016/j.cell.2018.04.019>.
42. Klaus, A., Martins, G.J., Paixao, V.B., Zhou, P., Paninski, L., and Costa, R.M. (2017). The Spatiotemporal Organization of the Striatum Encodes Action Space. *Neuron* 95, 1171–1180.e7.
43. Grillner, S., Robertson, B., and Kotaleski, J.H. (2020). Basal Ganglia–A Motion Perspective. *Compr. Physiol.* 10, 1241–1275.
44. Dudman, J.T., and Krakauer, J.W. (2016). The basal ganglia: from motor commands to the control of vigor. *Curr. Opin. Neurobiol.* 37, 158–166.
45. Miri, A., Warriner, C.L., Seely, J.S., Elsayed, G.F., Cunningham, J.P., Churchland, M.M., and Jessell, T.M. (2017). Behaviorally Selective Engagement of Short-Latency Effector Pathways by Motor Cortex. *Neuron* 95, 683–696.e11.
46. Sales-Carbonell, C., Taouali, W., Khalki, L., Pasquet, M.O., Petit, L.F., Moreau, T., Rueda-Orozco, P.E., and Robbe, D. (2018). No Discrete Start/Stop Signals in the Dorsal Striatum of Mice Performing a Learned Action. *Curr. Biol.* 28, 3044–3055.e5.
47. Moran, D.W., and Schwartz, A.B. (1999). Motor cortical representation of speed and direction during reaching. *J. Neurophysiol.* 82, 2676–2692.
48. Kaufman, M.T., Seely, J.S., Sussillo, D., Ryu, S.I., Shenoy, K.V., and Churchland, M.M. (2016). The Largest Response Component in the Motor Cortex Reflects Movement Timing but Not Movement Type. *eNeuro* 3, ENEURO.0085-16.2016. <https://doi.org/10.1523/ENEURO.0085-16.2016>.
49. Gallego, J.A., Perich, M.G., Naufel, S.N., Ethier, C., Solla, S.A., and Miller, L.E. (2018). Cortical population activity within a preserved neural manifold underlies multiple motor behaviors. *Nat. Commun.* 9, 4233.
50. Steinmetz, N.A., Aydin, C., Lebedeva, A., Okun, M., Pachitariu, M., Bauza, M., Beau, M., Bhagat, J., Böhm, C., Broux, M., et al. (2021). Neuropixels 2.0: A miniaturized high-density probe for stable, long-term brain recordings. *Science* 372, eabf4588. <https://doi.org/10.1126/science.abf4588>.
51. Park, J., Phillips, J.W., Guo, J.-Z., Martin, K.A., Hantman, A.W., and Dudman, J.T. (2022). Motor cortical output for skilled forelimb movement is selectively distributed across projection neuron classes. *Sci. Adv.* 8, eabj5167.
52. Ruder, L., Schina, R., Kanodia, H., Valencia-Garcia, S., Pivotto, C., and Arber, S. (2021). A functional map for diverse forelimb actions within brainstem circuitry. *Nature* 590, 445–450.
53. Azim, E., Jiang, J., Alstermark, B., and Jessell, T.M. (2014). Skilled reaching relies on a V2a propriospinal internal copy circuit. *Nature* 508, 357–363.
54. Guo, J.-Z., Graves, A.R., Guo, W.W., Zheng, J., Lee, A., Rodríguez-González, J., Li, N., Macklin, J.J., Phillips, J.W., Mensh, B.D., et al.

- (2015). Cortex commands the performance of skilled movement. *eLife* 4, e10774.
55. Tervo, D.G.R., Hwang, B.-Y., Viswanathan, S., Gaj, T., Lavzin, M., Ritola, K.D., Lindo, S., Michael, S., Kuleshova, E., Ojala, D., et al. (2016). A Designer AAV Variant Permits Efficient Retrograde Access to Projection Neurons. *Neuron* 92, 372–382.
  56. Winnubst, J., Bas, E., Ferreira, T.A., Wu, Z., Economo, M.N., Edson, P., Arthur, B.J., Bruns, C., Rokicki, K., Schauder, D., et al. (2019). Reconstruction of 1,000 Projection Neurons Reveals New Cell Types and Organization of Long-Range Connectivity in the Mouse Brain. *Cell* 179, 268–281.e13. <https://doi.org/10.1016/j.cell.2019.07.042>.
  57. Hunnicutt, B.J., Jongbloets, B.C., Birdsong, W.T., Gertz, K.J., Zhong, H., and Mao, T. (2016). A comprehensive excitatory input map of the striatum reveals novel functional organization. *eLife* 5, e19103. <https://doi.org/10.7554/eLife.19103>.
  58. Mahn, M., Gibor, L., Patil, P., Cohen-Kashi Malina, K., Oring, S., Printz, Y., Levy, R., Lampl, I., and Yizhar, O. (2018). High-efficiency optogenetic silencing with soma-targeted anion-conducting channelrhodopsins. *Nat. Commun.* 9, 4125.
  59. Foster, N.N., Barry, J., Korobkova, L., Garcia, L., Gao, L., Becerra, M., Sherafat, Y., Peng, B., Li, X., Choi, J.-H., et al. (2021). The mouse cortico-basal ganglia-thalamic network. *Nature* 598, 188–194.
  60. Yu, B.M., Cunningham, J.P., Santhanam, G., Ryu, S.I., Shenoy, K.V., and Sahani, M. (2009). Gaussian-process factor analysis for low-dimensional single-trial analysis of neural population activity. *J. Neurophysiol.* 102, 614–635.
  61. Fetz, E.E. (1994). Are movement parameters recognizably coded in the activity of single neurons? In *Movement Control*, P. Cordo and S. Harnad, eds. (Cambridge University Press), pp. 77–88.
  62. Gallego, J.A., Perich, M.G., Miller, L.E., and Solla, S.A. (2017). Neural Manifolds for the Control of Movement. *Neuron* 94, 978–984.
  63. Semedo, J.D., Zandvakili, A., Machens, C.K., Yu, B.M., and Kohn, A. (2019). Cortical Areas Interact through a Communication Subspace. *Neuron* 102, 249–259.e4.
  64. Perich, M.G., Gallego, J.A., and Miller, L.E. (2018). A neural population mechanism for rapid learning. *Neuron* 100, 964–976.e7.
  65. Abid, A., Zhang, M.J., Bagaria, V.K., and Zou, J. (2018). Exploring patterns enriched in a dataset with contrastive principal component analysis. *Nat. Commun.* 9, 2134.
  66. Kobak, D., Brendel, W., Constantinidis, C., Feierstein, C.E., Kepecs, A., Mainen, Z.F., Qi, X.-L., Romo, R., Uchida, N., and Machens, C.K. (2016). Demixed principal component analysis of neural population data. *eLife* 5, e10989. <https://doi.org/10.7554/eLife.10989>.
  67. Rueda-Orozco, P.E., and Robbe, D. (2015). The striatum multiplexes contextual and kinematic information to constrain motor habits execution. *Nat. Neurosci.* 18, 453–460.
  68. Yttri, E.A., and Dudman, J.T. (2016). Opponent and bidirectional control of movement velocity in the basal ganglia. *Nature* 533, 402–406.
  69. Mazzoni, P., Hristova, A., and Krakauer, J.W. (2007). Why don't we move faster? Parkinson's disease, movement vigor, and implicit motivation. *J. Neurosci.* 27, 7105–7116.
  70. Lemke, S.M., Ramanathan, D.S., Guo, L., Won, S.J., and Ganguly, K. (2019). Emergent modular neural control drives coordinated motor actions. *Nat. Neurosci.* 22, 1122–1131.
  71. Gao, P., Trautmann, E., Yu, B., Santhanam, G., Ryu, S., Shenoy, K., and Ganguly, S. (2017). A theory of multineuronal dimensionality, dynamics and measurement. Preprint at bioRxiv. <https://doi.org/10.1101/214262>.
  72. Fortunato, C., Bennasar-Vázquez, J., Park, J., Chang, J.C., Miller, L.E., Dudman, J.T., Perich, M.G., and Gallego, J.A. (2024). Nonlinear manifolds underlie neural population activity during behaviour. Preprint at bioRxiv. <https://doi.org/10.1101/2023.07.18.549575>.
  73. Lillicrap, T.P., and Scott, S.H. (2013). Preference distributions of primary motor cortex neurons reflect control solutions optimized for limb biomechanics. *Neuron* 77, 168–179.
  74. Jurado-Parras, M.-T., Safaie, M., Sarno, S., Louis, J., Karoutchi, C., Berret, B., and Robbe, D. (2020). The Dorsal Striatum Energizes Motor Routines. *Curr. Biol.* 30, 4362–4372.e6.
  75. Baraduc, P., Thobois, S., Gan, J., Broussolle, E., and Desmurget, M. (2013). A common optimization principle for motor execution in healthy subjects and parkinsonian patients. *J. Neurosci.* 33, 665–677.
  76. Morita, K., Im, S., and Kawaguchi, Y. (2019). Differential Striatal Axonal Arborizations of the Intratelencephalic and Pyramidal-Tract Neurons: Analysis of the Data in the MouseLight Database. *Front. Neural Circuits* 13, 71.
  77. Desmurget, M., and Turner, R.S. (2010). Motor sequences and the basal ganglia: kinematics, not habits. *J. Neurosci.* 30, 7685–7690.
  78. Horak, F.B., and Anderson, M.E. (1984). Influence of globus pallidus on arm movements in monkeys. II. Effects of stimulation. *J. Neurophysiol.* 52, 305–322.
  79. Tepper, J.M., Abercrombie, E.D., and Bolam, J.P. (2007). GABA and the basal ganglia: from molecules to systems. In *Progress in Brain Research* (Elsevier), p. 339.
  80. Yttri, E.A., and Dudman, J.T. (2018). A proposed circuit computation in basal ganglia: History-dependent gain. *Mov. Disord.* 33, 704–716.
  81. Wolff, S.B.E., Ko, R., and Ölveczky, B.P. (2022). Distinct roles for motor cortical and thalamic inputs to striatum during motor skill learning and execution. *Sci. Adv.* 8, eabk0231.
  82. Hwang, E.J., Dahlen, J.E., Hu, Y.Y., Aguilar, K., Yu, B., Mukundan, M., Mitani, A., and Komiyama, T. (2019). Disengagement of motor cortex from movement control during long-term learning. *Sci. Adv.* 5, eaay0001.
  83. Thura, D., and Cisek, P. (2017). The Basal Ganglia Do Not Select Reach Targets but Control the Urgency of Commitment. *Neuron* 95, 1160–1170.e5.
  84. DeLong, M.R., Alexander, G.E., Georgopoulos, A.P., Crutcher, M.D., Mitchell, S.J., and Richardson, R.T. (1984). Role of basal ganglia in limb movements. *Hum. Neurobiol.* 2, 235–244.
  85. Cisek, P. (2022). Evolution of behavioural control from chordates to primates. *Philos. Trans. R. Soc. Lond. B Biol. Sci.* 377, 20200522.
  86. Mizes, K.G.C., Lindsey, J., Escola, G.S., and Ölveczky, B.P. (2022). Similar striatal activity exerts different control over automatic and flexible motor sequences. Preprint at bioRxiv.
  87. Legaria, A.A., Licholai, J.A., and Kravitz, A.V. (2021). Fiber photometry does not reflect spiking activity in the striatum 1. *Methods* 152, 153.
  88. Owen, S.F., Berke, J.D., and Kreitzer, A.C. (2018). Fast-Spiking Interneurons Supply Feedforward Control of Bursting, Calcium, and Plasticity for Efficient Learning. *Cell* 172, 683–695.e15.
  89. Fobbs, W.C., Bariselli, S., Licholai, J.A., Miyazaki, N.L., Matikainen-Ankney, B.A., Creed, M.C., and Kravitz, A.V. (2020). Continuous Representations of Speed by Striatal Medium Spiny Neurons. *J. Neurosci.* 40, 1679–1688.
  90. Barbera, G., Liang, B., Zhang, L., Gerfen, C.R., Culurciello, E., Chen, R., Li, Y., and Lin, D.-T. (2016). Spatially Compact Neural Clusters in the Dorsal Striatum Encode Locomotion Relevant Information. *Neuron* 92, 202–213.
  91. Wei, Z., Lin, B.-J., Chen, T.-W., Daie, K., Svoboda, K., and Druckmann, S. (2020). A comparison of neuronal population dynamics measured with calcium imaging and electrophysiology. *PLoS Comput. Biol.* 16, e1008198. <https://doi.org/10.1371/journal.pcbi.1008198>.
  92. Stringer, C., Pachitariu, M., Steinmetz, N., Reddy, C.B., Carandini, M., and Harris, K.D. (2019). Spontaneous behaviors drive multidimensional, brainwide activity. *Science* 364, 255.

93. Musall, S., Kaufman, M.T., Juavinett, A.L., Gluf, S., and Churchland, A.K. (2019). Single-trial neural dynamics are dominated by richly varied movements. *Nat. Neurosci.* 22, 1677–1686.
94. Peters, A.J., Fabre, J.M.J., Steinmetz, N.A., Harris, K.D., and Carandini, M. (2021). Striatal activity topographically reflects cortical activity. *Nature* 591, 420–425.
95. Neafsey, E.J., Hull, C.D., and Buchwald, N.A. (1978). Preparation for movement in the cat. II. Unit activity in the basal ganglia and thalamus. *Electroencephalogr. Clin. Neurophysiol.* 44, 714–723.
96. Srivastava, N., Hinton, G., Krizhevsky, A., Sutskever, I., and Salakhutdinov, R. (2014). Dropout: a simple way to prevent neural networks from overfitting. *J Mach Learn Res.* 15, 1929–1958.
97. Banino, A., Barry, C., Uria, B., Blundell, C., Lillicrap, T., Mirowski, P., Pritzel, A., Chadwick, M.J., Degris, T., Modayil, J., et al. (2018). Vector-based navigation using grid-like representations in artificial agents. *Nature* 557, 429–433.
98. Dubreuil, A., Valente, A., Beiran, M., Mastrogiosse, F., and Ostoic, S. (2022). The role of population structure in computations through neural dynamics. *Nat. Neurosci.* 25, 783–794.
99. Chang, J.C., Perich, M.G., Miller, L.E., Gallego, J.A., and Clopath, C. (2024). De novo motor learning creates structure in neural activity that shapes adaptation. *Nat. Commun.* 15, 4084.
100. Safaie, M., Chang, J.C., Park, J., Miller, L.E., Dudman, J.T., Perich, M.G., and Gallego, J.A. (2022). Preserved neural population dynamics across animals performing similar behaviour. *Nature* 623, 765–771. <https://doi.org/10.1038/s41586-023-06714-0>.
101. Sauerbrei, B.A., Guo, J.-Z., Cohen, J.D., Mischiati, M., Guo, W., Kabra, M., Verma, N., Mensh, B., Branson, K., and Hantman, A.W. (2020). Cortical pattern generation during dexterous movement is input-driven. *Nature* 577, 386–391.
102. Jiang, W.-C., Xu, S., and Dudman, J.T. (2022). Hippocampal representations of foraging trajectories depend upon spatial context. *Nat. Neurosci.* 25, 1693–1705.
103. Dacre, J., Colligan, M., Clarke, T., Ammer, J.J., Schiemann, J., Chamosa-Pino, V., Claudi, F., Harston, J.A., Eleftheriou, C., Pakan, J.M.P., et al. (2021). A cerebellar-thalamocortical pathway drives behavioral context-dependent movement initiation. *Neuron* 109, 2326–2338.e8.
104. Wang, X., Chou, X.-L., Zhang, L.I., and Tao, H.W. (2020). Zona Incerta: An Integrative Node for Global Behavioral Modulation. *Trends Neurosci.* 43, 82–87.
105. Tervo, D.G.R., Kuleshova, E., Manakov, M., Proskurin, M., Karlsson, M., Lustig, A., Behnam, R., and Karpova, A.Y. (2021). The anterior cingulate cortex directs exploration of alternative strategies. *Neuron* 109, 1876–1887.e6.
106. Li, B. (2019). Central amygdala cells for learning and expressing aversive emotional memories. *Curr. Opin. Behav. Sci.* 26, 40–45.
107. Averbeck, B.B., and Costa, V.D. (2017). Motivational neural circuits underlying reinforcement learning. *Nat. Neurosci.* 20, 505–512.
108. Taylor, J.A., Krakauer, J.W., and Ivry, R.B. (2014). Explicit and implicit contributions to learning in a sensorimotor adaptation task. *J. Neurosci.* 34, 3023–3032.
109. Krakauer, J.W., Hadjiosif, A.M., Xu, J., Wong, A.L., and Haith, A.M. (2019). Motor Learning. *Compr. Physiol.* 9, 613–663. <https://doi.org/10.1002/cphy.c170043>.
110. Otchy, T.M., Wolff, S.B.E., Rhee, J.Y., Pehlevan, C., Kawai, R., Kempf, A., Gobes, S.M.H., and Ölveczky, B.P. (2015). Acute off-target effects of neural circuit manipulations. *Nature* 528, 358–363.
111. Whishaw, I.Q. (2000). Loss of the innate cortical engram for action patterns used in skilled reaching and the development of behavioral compensation following motor cortex lesions in the rat. *Neuropharmacology* 39, 788–805.
112. Nicholas, M.A., and Yttri, E.A. (2024). Motor cortex is responsible for motoric dynamics in striatum and the execution of both skilled and unskilled actions. *Neuron* 112, 3486–3501.e5. <https://doi.org/10.1016/j.neuron.2024.07.022>.
113. Stroud, J.P., Porter, M.A., Hennequin, G., and Vogels, T.P. (2018). Motor primitives in space and time via targeted gain modulation in cortical networks. *Nat. Neurosci.* 21, 1774–1783.
114. Blumberg, M.S., and Adolph, K.E. (2023). Protracted development of motor cortex constrains rich interpretations of infant cognition. *Trends Cogn. Sci.* 27, 233–245.
115. Glanz, R.M., Sokoloff, G., and Blumberg, M.S. (2023). Neural decoding reveals specialized kinematic tuning after an abrupt cortical transition. *Cell Rep.* 42, 113119.
116. Pachitariu, M., Sridhar, S., Pennington, J., and Stringer, C. (2024). Spike sorting with Kilosort4. *Nat. Methods* 21, 914–921.
117. Pedregosa, F., Varoquaux, G., Gramfort, A., Michel, V., Thirion, B., Grisel, O., Blondel, M., Louppe, G., Prettenhofer, P., Weiss, R., et al. (2011). Scikit-learn: Machine Learning in Python. *J. Mach. Learn. Res.* 12, 2825–2830. <https://doi.org/10.5555/1953048.2078195>.
118. Nath, T., Mathis, A., Chen, A.C., Patel, A., Bethge, M., and Mathis, M.W. (2019). Using DeepLabCut for 3D markerless pose estimation across species and behaviors. *Nat. Protoc.* 14, 2152–2176.
119. Bogovic, J.A., Hanslovsky, P., Wong, A., and Saalfeld, S. (2016). Robust registration of calcium images by learned contrast synthesis. In 2016 IEEE 13th International Symposium on Biomedical Imaging (ISBI), pp. 1123–1126.
120. Mante, V., Sussillo, D., Shenoy, K.V., and Newsome, W.T. (2013). Context-dependent computation by recurrent dynamics in prefrontal cortex. *Nature* 503, 78–84.
121. Economo, M.N., Viswanathan, S., Tasic, B., Bas, E., Winnubst, J., Menon, V., Graybuck, L.T., Nguyen, T.N., Smith, K.A., Yao, Z., et al. (2018). Distinct descending motor cortex pathways and their roles in movement. *Nature* 563, 79–84.
122. Safaie, M., Chang, J.C., Park, J., Miller, L.E., Dudman, J.T., Perich, M.G., and Gallego, J.A. (2023). Preserved neural dynamics across animals performing similar behaviour. *Nature* 623, 765–771. <https://doi.org/10.1038/s41586-023-06714-0>.
123. Glaser, J.I., Benjamin, A.S., Chowdhury, R.H., Perich, M.G., Miller, L.E., and Kording, K.P. (2020). Machine Learning for Neural Decoding. *eNeuro* 7, ENEURO.0506-19.2020. <https://doi.org/10.1523/ENEURO.0506-19.2020>.

## STAR★METHODS

## KEY RESOURCES TABLE

REAGENT or RESOURCE	SOURCE	IDENTIFIER
Experimental models: Organisms/strains		
Slc17a7(Vglut1)-IRES2-Cre-D	Jackson Laboratory	037512
rAAV2retro-hSyn-SIO-stGtACR2-KV-eGFP <sup>58</sup>	Janelia Viral Tools	N/A
N-butyl-diethanolamine	Sigma-Aldrich	471240
Triton X-100	Sigma-Aldrich	X100
TO-PRO-3	Thermo Fisher Scientific	R37170
Nicotinamide	Sigma-Aldrich	N3376
Antipyrine	Sigma-Aldrich	A5882
Dil	Thermo Fisher Scientific	V22885
Software and algorithms		
Mouse joystick interface python	Janelia Experimental Technology	<a href="https://github.com/janelia-pypi/mouse_joystick_interface_python">https://github.com/janelia-pypi/mouse_joystick_interface_python</a>
SpikeGLX	Bill Karsh at Janelia Research Campus	<a href="http://billkarsh.github.io/SpikeGLX/">http://billkarsh.github.io/SpikeGLX/</a>
Kilosort	Pachitariu et al. <sup>116</sup>	<a href="https://github.com/MouseLand/Kilosort">https://github.com/MouseLand/Kilosort</a>
Phy	<a href="https://www.ucl.ac.uk/cortexlab">https://www.ucl.ac.uk/cortexlab</a>	<a href="https://github.com/cortex-lab/phy">https://github.com/cortex-lab/phy</a>
MATLAB	Mathworks	<a href="https://www.mathworks.com/">https://www.mathworks.com/</a>
FIJI/ImageJ	NIH	<a href="https://fiji.sc/">https://fiji.sc/</a>
Python 3.0	Python Software Foundation	<a href="https://www.python.org/">https://www.python.org/</a>
Illustrator 2024	Adobe	<a href="https://www.adobe.com/products/illustrator.html">https://www.adobe.com/products/illustrator.html</a>
Scikit-learn	Pedregosa et al. <sup>117</sup>	<a href="https://scikit-learn.org/stable/">https://scikit-learn.org/stable/</a>
cPCA	Abid et al. <sup>65</sup>	<a href="https://github.com/abidlabs/contrastive">https://github.com/abidlabs/contrastive</a>
dPCA	Kobak et al. <sup>66</sup>	<a href="http://github.com/machenslab/dPCA">http://github.com/machenslab/dPCA</a>
GPFA	Yu et al. <sup>60</sup>	<a href="https://users.ece.cmu.edu/~byronyu/software.shtml">https://users.ece.cmu.edu/~byronyu/software.shtml</a>
Reduced rank regression	Semedo et al. <sup>63</sup>	<a href="https://github.com/joao-semedo/communication-subspace">https://github.com/joao-semedo/communication-subspace</a>
DeepLabCut	Nath et al. <sup>118</sup>	<a href="https://github.com/DeepLabCut/DeepLabCut">https://github.com/DeepLabCut/DeepLabCut</a>
BigWarp	Bogovic et al. <sup>119</sup>	<a href="https://imagej.net/plugins/bigwarp">https://imagej.net/plugins/bigwarp</a>
Camera Calibration Toolbox for Matlab	CaltechDATA	<a href="https://data.caltech.edu/records/jx9cx-fdh55">https://data.caltech.edu/records/jx9cx-fdh55</a>
Neuropixels recording dataset	This paper	<a href="https://doi.org/10.25378/janelia.28025282">https://doi.org/10.25378/janelia.28025282</a>
Analysis software	GitHub	<a href="https://doi.org/10.25378/janelia.28025357">https://doi.org/10.25378/janelia.28025357</a>
Hardware		
Mouse joystick apparatus parts (CAD)	Janelia Experimental Technology	<a href="https://www.dropbox.com/scl/folder/y4ozvuk3mgx61g19stthj/h?rlkey=s6soot4oazr9520nij5pgt1lx&amp;dl=0">https://www.dropbox.com/scl/folder/y4ozvuk3mgx61g19stthj/h?rlkey=s6soot4oazr9520nij5pgt1lx&amp;dl=0</a>
Stepper Motor 1	Pololu	<a href="https://www.pololu.com/product/1204">https://www.pololu.com/product/1204</a>
Stepper Motor 2	Pololu	<a href="https://www.pololu.com/product/2267">https://www.pololu.com/product/2267</a>
Rotary encoder	JTEKT Electronics	<a href="https://jtektele.in/Product/Incremental-Rotary-Encoder/TRD-MX1000AD">https://jtektele.in/Product/Incremental-Rotary-Encoder/TRD-MX1000AD</a>
USB3 Camera	Teledyne FLIR	<a href="https://www.flir.com/products/flea3-usb3/?model=FL3-U3-13E4M-C&amp;vertical-machine+vision&amp;segment=iis">https://www.flir.com/products/flea3-usb3/?model=FL3-U3-13E4M-C&amp;vertical-machine+vision&amp;segment=iis</a>

## EXPERIMENTAL MODEL AND STUDY PARTICIPANT DETAILS

All handling of animals and procedures were performed in strict accordance with the Janelia Research Campus Institutional Animal Care and Use Committee (IACUC) and the standards of the Association for Assessment and Accreditation of Laboratory Animal Care

(AAALAC). Male and female mice, typically aged 8 to 16 weeks at time of surgery, were used in this study. Mice were water restricted (1 to 1.5 ml of water/day) with daily health checks. Water restriction was eased if mice fell below 75% of their original body weight. Slc17a7-Cre (VGAT1-Cre) mice were generated by the Janelia Research Campus Gene Targeting and Transgenics Facility. Behavioral and neural data were taken from a total of 5 Slc17a7-Cre mice.

## METHOD DETAILS

### A novel joystick apparatus

The joystick made of stainless steel was connected to two stepper motors that provided rotation in the pitch and yaw. A rotary encoder tracked the stepper motor attached to the joystick, allowing us to infer the joystick kinematics, such as the pull distance. The joystick could be robotically positioned to one of two yaw locations on an equidistant arc in front of the head-fixed mouse. The joystick was then rotated into a pitch angle that was within the grasp of a head-fixed mouse. An auditory cue was delivered indicating when the joystick was in position and the task of the mouse was to reach out to the correct yaw target location, grab the joystick, and pull along the pitch axis past a specified threshold (5mm). The pitch motor could be used to set a variable load by controlling the amount of current to the motor windings. The pitch motor's holding load, which is the amount of force needed in order to move the motor one full step when the windings are energized but the rotor is stationary, was calibrated with a force gauge and translated to the force required to move the joystick. In these experiments we selected a 3g or 12g requirement. The CAD design files for constructing the joystick hardware can also be downloaded from: <https://www.dropbox.com/scl/f0/y4ozvuk3mgx61g19stthj/h?rkey=s6ssoot4oazr9520nij5pgt1lx&dl=0>. All joystick operations according to the user-defined task structure were programmatically controlled using a custom-written open source python package: [https://github.com/janelia-pypi/mouse\\_joystick\\_interface\\_python](https://github.com/janelia-pypi/mouse_joystick_interface_python). Additional details and other previously published hardware and software and analysis code will all be found and maintained at: <https://dudlab.notion.site/Conjoint-specification-of-action-in-neocortex-and-striatum-cebef9fc306947139f0ee70ce2dadeaa?pvs=4>.

### Training and performance in the Reach-to-Grasp task

Mice were trained for 2-6 weeks approximately 0.5 to 1 h every day before the initial data acquisition. For the first few days mice were acclimated to head fixation and the water spout that delivered drops of sweetened water. Once habituated with head fixation and water consumption the joystick was initially positioned in close proximity (5mm) to the resting right hand of the mice to facilitate discovery of the joystick with spontaneous limb movements. In the early phase of training, the pull threshold (<2mm) and load (<1g) were set to be low such that a slight pull triggered an immediate water reward. As mice learned to reach and pull the joystick, we gradually adjusted the task parameters - the initial position of the joystick (5 to 20mm from the resting hand), pull threshold (2 to 5mm), pull load (1 to 12g), and the delay for water delivery (0 to 1s). When the mice achieved an expert level performance (>150 successful trials in 60 min) with the adjusted parameters, we introduced the block design, in which mice performed two repetitions of the four joystick location (left; 5°, right; -15°) and pull load (Low; 3g, High; 12g pairs - 1) 5°/3g, 2) 5°/12g, 3) -15°/3g, 4) -15°/12g. All behavioral and neural data were taken when mice achieved an expert level with the varying task parameters. Each trial began with positioning of the joystick and a brief tone that signals the trial initiation, and the trial ended with a successful pull (> 5mm). Trials with incorrect responses (e.g., pushing the joystick past a threshold, 5mm) or timeout (the lack of pull or push for 10 s) were marked as unsuccessful. Within the response time window (10 s), during which the joystick was kept still at the set position, mice could initiate reaching voluntarily. At the end of each trial the joystick was retracted away from the mice and returned to the home position to be placed back to the set position for the next trial after the inter-trial interval (7 s). A transition to the next block occurred after 20 successful trials within the current block.

### Silencing of MO<sub>p</sub> → STR or MO<sub>s</sub> → STR projection neurons

To examine the behavioral effect of silencing MO<sub>p</sub> → STR or MO<sub>s</sub> → STR projection neurons, rAAV2retro-hSyn-SIO-stGtACR2-KV-eGFP [3.0 × 10<sup>12</sup> genome copies (GC)/ml] was injected to the dorsal striatum bilaterally (relative to lambda: 0.5 mm anterior; ±1.7 mm lateral; 2.8, 2.6, 2.4 mm deep; 30 nl per depth), labeling neurons projecting to the dorsal striatum. Viruses were obtained from Janelia Viral Tools (<http://www.janelia.org/support-team/viral-tools>). During corticostriatal inactivation sessions, approximately 25% of the total trials were randomly selected as inactivation trials, and a single pulse 473-nm bilateral laser was triggered during the inter-trial interval and terminated either by trial completion or after 4 seconds. The timing of laser onset varied from trial to trial (2.74 ± 1.2 s (median ± std) relative to the joystick placement at the target location) and was unpredictable.

### Histology

Following the completion of all experiments, the mice were perfused with 40 ml of cold PBS (pH 7.4) containing heparin (20 U/ml) at a rate of approximately 10 ml/min. The brains were then fixed using cold 4% paraformaldehyde (PFA). After extraction, the brains were further fixed in 4% PFA for 24 hours. The fixed brains were then delipidated for a week using the CUBIC-L cocktail, which is composed of 10/10% (w/w) N-butyldeethanolamine and Triton X-100. Following delipidation, the brains were counterstained with TO-PRO-3 (Thermo Fisher Scientific) for one day. Subsequently, the brains were made transparent using the CUBIC-R cocktail, consisting of 45/30% (w/w) antipyrine/nicotinamide, for two days. Finally, the cleared brains were imaged using fluorescence light sheet microscopy (Zeiss Lightsheet Z.1) to visualize GtACR2 expression (eGFP), probe tracks (Dil), and nuclear counterstaining

(TO-PRO-3). The imaged 3D brain volumes were aligned to a standardized brain coordinate system [Allen Anatomical Template (AAT)] using a semi-manual landmark-based method (big warp) to validate the probe tracks in the target regions (MOp, STR, and MOs/ACA).

## QUANTIFICATION AND STATISTICAL ANALYSIS

No explicit methods were used to estimate population sizes for expected effects beyond practical estimates standard across the field; distribution tests were used where relevant; most often results were confirmed with non-parametric tests where relevant.

### Extraction of 3-D hand and joystick trajectories using DeepLabCut

Two high-speed monochrome USB 3.0 cameras (FL3-U3-13E4M-C) equipped with 6- to 15-mm (f/1.4) lenses were positioned perpendicularly: one in front and one to the right of the animal. Both cameras were illuminated by a near-infrared light-emitting diode (LED) light source. The cameras were synchronized to capture frames at a rate of 250 Hz, providing a temporal resolution of 4 ms. We conducted stereo triangulation using the Camera Calibration Toolbox for Matlab (see the [key resources table](#)). DeepLabCut was trained to track three specific points: the leftmost and rightmost fingers, and the centroid of the hand. Additionally, two points were annotated on the joystick—at the top and the middle—to track its movement. We labeled approximately 300 frames per each view which led to successful tracking of all the annotated points. 3-D reconstruction of hand and joystick trajectories was computed on the 2-D pose estimation data from DeepLabCut using the calibrated parameters acquired by stereo triangulation, which also converted the pixel-wise positions into real-world units (mm).

### Extracellular electrophysiological recording

Before recordings, a craniotomy was made over the recording sites (MOp: 0.5 mm anterior, -1.7 mm lateral; MOs/ACA: 1.0 mm anterior, -0.3 mm lateral relative to bregma) at least 12 hours before recording under isoflurane anesthesia. All recordings were taken from the left hemisphere contralateral to the right forelimb that mice used to perform the task. The probes were centered above the craniotomies and lowered with ~10 degree angle from the axis perpendicular to the skull surface at a speed of 0.2 mm/min. The tip of the MOp/STR Neuropixels probe was located at ~4.2 mm ventral, while the MOs/ACA probe was lowered ~1.5 mm ventral from the pial surface. Before each insertion surface of each probe was coated with CM-Dil (Invitrogen), a read fixable lipophilic dye, for histological verification of probe tracks. Exposed brain tissue was kept moist with phosphate-buffered saline (PBS) at all times, and craniotomy sites were covered with Kwik-Sil elastomer (World Precision Instruments) outside of the recording session. All recordings were made with open-source software SpikeGLX (<http://billkarsh.github.io/SpikeGLX/>). Spike sorting was performed using the Kilosort2 (<https://github.com/MouseLand/Kilosort>) template matching and clustering algorithms with manual curation of the detected spikes using Phy (<https://github.com/cortex-lab/phy>).

### Gaussian Process Factor Analysis

We used GPFA to extract smooth, low-dimensional neural trajectories that summarize the activity recorded simultaneously from many neurons on individual trials (Figure 5). Let  $y_{:,t} \in \mathbb{R}^{q \times 1}$  represent the high-dimensional vector of square-rooted spike counts recorded at time point  $t = 1, \dots, T$ , where  $q$  is the number of neurons recorded simultaneously. The goal is to extract a corresponding low-dimensional latent neural state  $x_{:,t} \in \mathbb{R}^{p \times 1}$  at each time point, with  $p$  being the dimensionality of the state space ( $p < q$ ). We define a linear-Gaussian relationship between the observations  $y_{:,t}$  and neural states  $x_{:,t}$  as follows:

$$[y_{:,t} = Cx_{:,t} + d + \epsilon_t]$$

where  $C \in \mathbb{R}^{q \times p}$ ,  $d \in \mathbb{R}^{q \times 1}$ , and  $R \in \mathbb{R}^{q \times q}$  are the model parameters to be learned. Similar to Factor Analysis (FA), the covariance matrix  $R$  was constrained to be diagonal, with each diagonal element representing the independent noise variance for each neuron. The neural states  $x_{:,t}$  at different time points are related through Gaussian processes, which enforce the idea that the neural trajectories should be smooth.

### Reduced Rank Regression

To understand trial-to-trial fluctuations in neuronal populations, a linear model  $Y = XB$  was used, where  $X$  represents the residual activity (mean-subtracted activity) in the source population and  $Y$  in the target population. The coefficient matrix  $B$  is determined using ordinary least-squares (OLS) regression:

$$B_{OLS} = (X^T X)^{-1} X^T$$

To prevent overfitting, ridge regression was employed, modifying the OLS solution to include a regularization term:

$$B_{Ridge} = (X^T X + \lambda I)^{-1} X^T Y$$

where  $\lambda$  is a regularization parameter optimized via cross-validation.

To explore if the target population can be predicted using a subspace of the source population, RRR was applied (Figure 4). RRR constrains  $B$  to a given rank  $m$ , solved using Singular Value Decomposition (SVD):

$$B_{RRR} = B_{OLS}V_m^T$$

Here,  $V_m$  contains the top  $m$  principal components of  $Y_{OLS} = XB_{OLS}$ . The predicted target population activity using RRR is:

$$\hat{Y}_{RRR} = XB_{OLS}V_m^T$$

### Dimensionality estimate

Linear dimensionality was estimated as described previously using principal component analysis (Figure 5).<sup>72</sup> We report the max dimensionality across recorded datasets; however, the difference between STR and MOp were robust across a broad range of re-sampled population sizes using 10-fold resampling.

### Principal Component Analysis and contrastive Principal Component Analysis

The encoding model described in Figure 1 and the introduction can be considered a “ground truth” model that can be used to evaluate the extent to which any given analysis can discover the underlying structure present, by construction, in the simulated data. As we describe the encoding model has 2 distinct, but important features. One, there is a stereotyped and large modulation of activity across many of the neurons associated with the initiation of a movement that is uncorrelated with the detailed encoding of trajectory angle and force (as previously articulated in primate MOp<sup>48</sup>). Second, there are changes in the identity of the most active neurons reflecting changes in trajectory direction and changes in the scaling of modulation of activity reflecting changes in movement force. As expected the general modulation of all neurons by movement initiation is the largest source of variance in the dataset and as a result principal component analysis (PCA) is dominated by this rich spatiotemporal variability (Figure S5). Similarly, GPFA (which in data of this sort can be nearly equivalent to PCA+temporal smoothing) is also dominated by these spatiotemporal dynamics (Figure 4). However, we know in the case of the constructed encoding model that there are differences associated with different trajectory angles and thus the question is what analysis might be best able to reveal those differences. One good candidate that makes relatively minimal assumptions is to use an approach such as contrastive PCA (cPCA).<sup>65</sup> cPCA is much like PCA but with one additional step - it tries to remove the shared covariance common to all conditions to reveal variance in the marginals of what changes across conditions. Indeed, we can accomplish this effectively in this data by either computing PCA over the difference in PSTHs across conditions or by subtracting covariance matrices of the mean PSTHs. Examples are shown in Figure S5 where cPCA clearly reveals the known differences in the encoding model across conditions. As we note in the text this has close similarities (and in these datasets is essentially indistinguishable in the conclusions drawn) to other commonly used methods such as targeted dimensionality reduction,<sup>120</sup> coding dimensions,<sup>121</sup> and demixed PCA.<sup>66</sup> As an example we show the results of analyzing neural data with dPCA in Figure S5 for comparison. Differences were quantified as the rotation component of a Procrustes transformation across trajectories which does an excellent job of aligning neural trajectories without disrupting the capacity to decode movement kinematics.<sup>122</sup>

### Neural decoding of 3D hand trajectories with Kalman filter

Our Kalman filter for neural decoding consisted of the state model and the observation model (Figure 5).<sup>123</sup> The state model captures the linear function and its uncertainty, based on which the state variables (3D hand trajectories) evolve from time  $t-1$  to  $t$  with 20-ms timesteps. The linear relationship between the state variables and the activity of neurons is captured by the observation model. Parameters specifying the state and observation models that are jointly Gaussian were learned in the training phase. In the test phase, the held-out hand trajectories were estimated recursively through one-step prediction and measurement update. The model performance was evaluated as the coefficient of determination ( $R^2$ ) between the actual and estimated trajectories.

The state model is defined as:

$$P(z_t|z_{t-1}) \sim N(A \cdot z_{t-1}, Q)$$

where  $z$  is a three dimensional vector containing state variables (3D hand coordinates) per timestep (20 ms).  $A$  is a matrix that describes transition of state variables between timesteps.  $Q$  is the covariance matrix that characterizes the uncertainty around the estimated state transition. The initial hand coordinates  $z_1$  was estimated as the sample mean and covariance from the training dataset.

$$P(z_1) \sim N(\pi, V)$$

The observation model is defined as:

$$P(x_t|z_t) \sim N(C \cdot z_t, R)$$

where  $x$  is a  $n$ -dimensional vector ( $n$  = the number of neurons) containing the spike count of neurons per timestep.  $C$  is a matrix that captures the linear mapping between the state and observation variables.  $R$  is the covariance matrix that characterizes the uncertainty around the estimated observation variables. The model parameters  $\theta = \{A, Q, \pi, V, C, R\}$  were estimated analytically on the training dataset during the training phase. In the test phase, the 3D hand trajectories of the held-out trials were estimated recursively following one-step prediction and measurement update.

One-step prediction:

$$P(z_t | \{x\}_1^{t-1}) = \int P(z_t | z_{t-1}) P(z_{t-1} | \{x\}_1^{t-1}) dz_{t-1}$$

Measurement update:

$$P(z_t | \{x\}_1^t) = \frac{P(x_t | z_t) P(z_t | \{x\}_1^{t-1})}{P(x_t | \{x\}_1^{t-1})}$$

A leave-one-out cross-validation was used to train and evaluate the model from separate datasets. When there are two (MOp, dSTR) or more (MOp, dSTR, MOs/ACA) simultaneously recorded populations, we trained and tested the decoder with or without resampling the neurons from each population. The purpose of resampling was to match the number of neurons when comparing the decoder performance between populations. Resampling was repeated for a total of 30 iterations. Models trained with all neurons without resampling provided an approximate upper limit of decoder accuracy.

### Random forest classifier

To compare discriminative encoding of trial types (four location and load combinations) across neural populations, we trained decision tree-based random forest classifiers via the scikit-learn's RandomForestClassifier implementation. Binned spike count data were organized in 3D matrices whose dimensions were the number of neurons, the number of time bins, and the number of trials. Only data from trials with successful reach-to-grasp performance were used to train and test classifiers. Stratified 5-fold cross validation (scikit-learn) was used to train and test classifiers with balanced distribution of the four trial types within each fold. For inter-regional comparison of decoding accuracy the number of neurons were matched across simultaneously recorded neural populations by random sampling over 100 times. Data shown in Figure 5C represent the median decoding accuracy of 100 accuracy values calculated from resampled data. Python codes used for training and testing random forest classifiers can be found here: [https://github.com/jup36/MatlabNeuralDataPipeline/tree/master/neural\\_encoding\\_trial\\_types\\_js2p0](https://github.com/jup36/MatlabNeuralDataPipeline/tree/master/neural_encoding_trial_types_js2p0).

### Characterization of individual neuronal encoding of trial types with $d'$

To quantify the degree to which the  $2 \times 2$  trial types of joystick loads (low vs. high) and positions (left vs. right) are encoded by individual neuronal firing rates, the discriminability index ( $d'$ ) was computed for each trial type (Figure 6). The individual neuronal mean firing rate of each trial type was subtracted by the mean of the rest of the trial types with normalization by the sum of standard deviations.

$$\Delta FR_{Trial\ type} = \frac{(FR_{Trial\ type} - FR_{Rest})}{(\sigma_{Trial\ type} + \sigma_{Rest})}$$

Applying the above equation for each of the four trial types yielded four  $\Delta FR$  values that were projected onto four vectors  $[1\ 1]^T$ ,  $[1, -1]^T$ ,  $[-1, -1]^T$ ,  $[-1, 1]^T$ . These vectors correspond to the four location-load pairs, namely, right-high, right-low, left-low, and left-high, respectively. The sum of projected vectors yields 2D coordinates on an 'encoding space' that characterizes the neuronal encoding of the joystick location (horizontal axis) and required force (vertical axis). The length of this resultant vector was taken as the neuronal trial-type discriminability score,  $d'$ . Continuous time  $d'$  scores (trajectory) was computed for each 20-ms bin spanning -1 to 1 s relative to the reach start.  $d'$  captured the preferential tuning property of individual neurons and its visualization within the 2D  $d'$  space.

For a statistical significance test, trial-shuffled  $d'$  trajectories were obtained with 1000 shuffles, and their maximum distances from the origin (0, 0) were calculated. The 95% confidence interval was estimated from the maximum distance distribution (mean + 2 · std). If a neuron's actual  $d'$  trajectory (i.e., without trial shuffling) had crossing(s) of this 95% confidence interval in one or more time bin(s), the neuron was considered to encode a task variable. The neuronal encoding was further characterized by subdividing the 2D encoding space by the eight equi-spaced vectors. Single units were classified into the 8 classes by spotting which of the 8 equi-spaced vectors its max  $d'$  coordinates are best aligned to.

### Committee decoder design

To assess the contribution of distinct neural populations to forelimb movement, we used a linear decoder to estimate the trial by trial parameters of reach angle and pull force from integrated neural activity (windows: ) during the reach and pull phases, respectively. The decoded estimates were then correlated with the actual joystick trajectories. The decoder seeks to identify an optimal (minimization of least squares) linear mapping ( $W_{decode}$ ; dimension Neurons x 1) between the neural population activity ( $R$ ; dimension Trials x Neurons) and the chosen behavioral parameters (max pull force or reach angle;  $B$  dimensions Trials x 1):

$$B = R \cdot W_{decode}$$

We solve for  $W_{decode}$  as the mean of the estimates  $W$  computed (using *pseudoinverse(activity) \* data*) from random batches of training trials (batch size: 75% population; batch number: 200–500; model: batch size: 30; batch num: 200). For cross validation, we evaluate the decoder on total trials or held out trials to look for good generalization of  $W_{decode}$  performance. Based upon ground truth models (see below) we found the best evaluation of decoder performance to be the slope of the relationship between predicted and observed data for reach angle and pull force separately (example in Figures 7 and S8). For evaluation of decoding quality from a given population we use root mean squared error (RMSE; Figure 8) which provides an unsigned estimate of fit quality. Estimates of average pairwise correlations are obtained by taking the mean of correlations in the upper triangular portion of correlation matrix of integrated activity per trial.

### Encoding simulated data

To produce the activity dynamics simulated in Figures 1 and S1 we generated simulated networks (typical N=120 units) in which activity profiles were produced as a combination of random lags at the typical timing of reach onset or pull onset, variable durations, and an independent response timed to the latency of reward delivery (gain: Poisson random lag:  $\lambda=3$ ). Individual profiles were generated as a combination of a half Gaussian rise (median: 45; uniform random: [25:65] & median: 80; range: [25:300]) and a half Gaussian decay (median: 150 & median: 200). Lags were determined as a single sample per unit from a Poisson random distribution determined by  $\lambda=1:120$  and  $\lambda=9:9:1080$ . Tuning to reach angle and pull force were generated from cosine tunings and uniform random monotonic gain tuning (uniform random, range=[0:0.8]), respectively (as in canonical motor direction tuning analysis<sup>47</sup> and prior observations in mice, e.g. Panigrahi et al.<sup>39</sup>). Observations reported are consistent across a wide range of parameter values.

### Two population decoding simulated data

To produce the activity dynamics simulated in Figure 7 we simulated the total spike count per trial for N=100 trials. To produce tuned activity we considered inputs, independent across the two populations termed **m** and **s**. Each unit received noisy input tuned across a range of monotonic gains - uniform distributed between [-0.15 and 0.85] - and a normally distributed source of noise  $N(0, \sigma=1)$ . 15% of the coupling between **m** and **s** layers is determined by the matrix  $W_{m,s}$ . We considered several different structures. With the exception of the random  $W_{m,s}$  matrix (uniform: [-0.5:0.5]) all matrices were produced by a Gaussian distributed weights with an excitatory and inhibitory component uniformly shifted by one unit across the population. Gaussian excitatory and inhibitory kernels had the following dispersion parameterizations:

```
type 'center_surround'
E: σ=2
I: σ=16
type 'topographic'
E: σ=2
case 'distributed'
E_center : σ=2
E_surround : σ={3,4}
I_center : σ=10
I_surround : σ=10
```

Example code for simulations will be made available at: <https://dudlab.notion.site/Conjoint-specification-of-action-in-neocortex-and-striatum-cebef9fc306947139f0ee70ce2dadeaa?pvs=4>.

**Supplemental information**

**Conjoint specification of action by neocortex  
and striatum**

**Junchol Park, Peter Polidoro, Catia Fortunato, Jon Arnold, Brett Mensh, Juan A. Gallego, and Joshua T. Dudman**

# **Supplemental Materials for Park et al.**

Supplemental Methods

Supplemental Figures S1 to S8

Table S1

Supplemental Figure 1

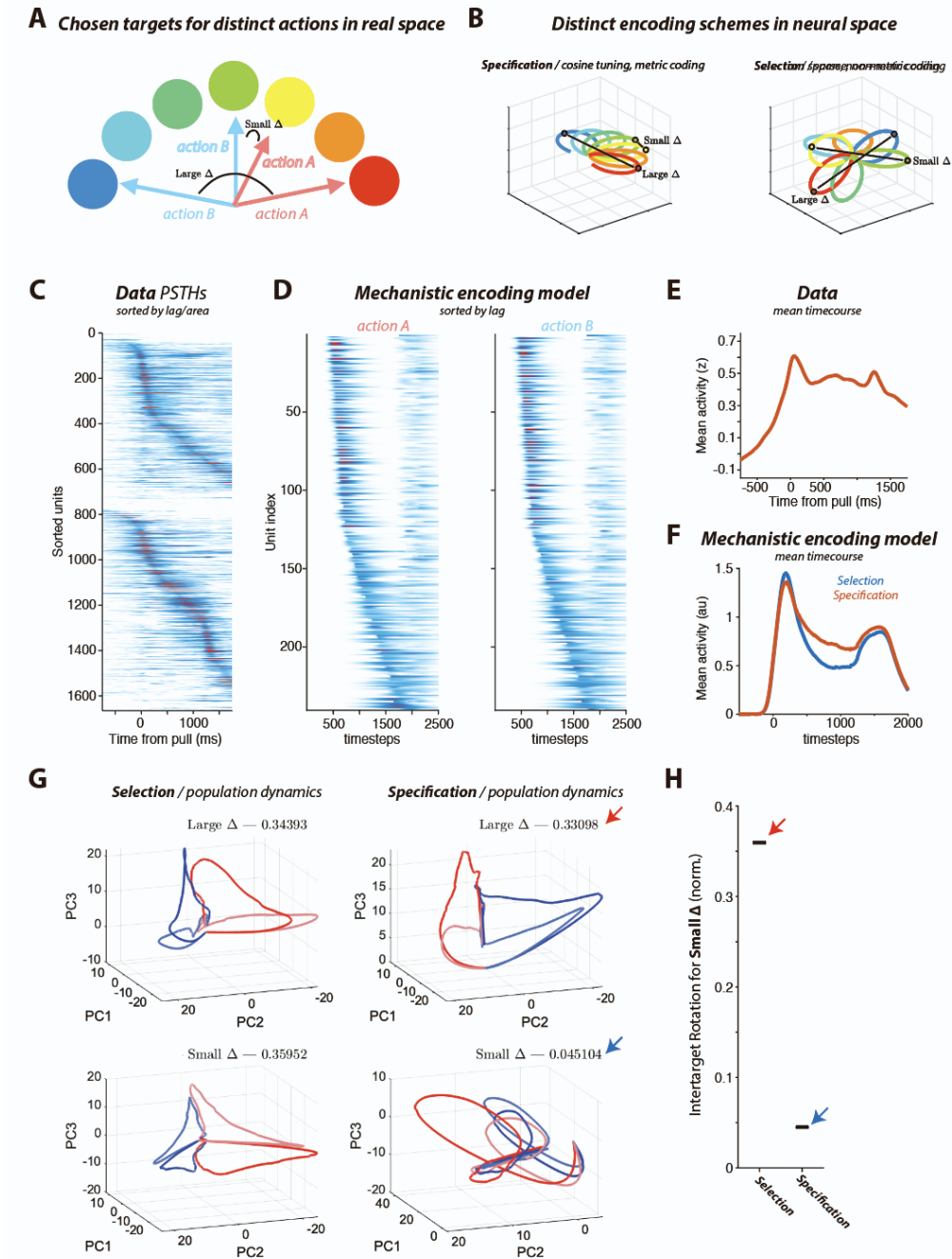


**Figure S1. Elaboration on the encoding model, related to Figure 1**

**A**, Consider a set of different targets which two actions (A & B) may target, e.g. a reaching movement of the forelimb. We are interested in comparing the expected neural activity differences between two actions as a function of whether those actions are similar in real space (small intertarget angle) as opposed to far apart. **B**, we consider two different kinds of encoding schemes in the space of neural activity dynamics (3 dimensions illustrated; color code as in **A**). In the case of a specification or “controller” model (left) neural activity mimics the real space of different actions - e.g. cosine tuning of activity to reach angle laying on a flat manifold in neural space). The power of a sparse coding scheme useful for a “selector” model is that activity is projected in separate directions for any given action in the space. This allows all actions to be similarly far in their encoding in neural space (i.e. a sparse code). Thus, for similar actions in a specification model the neural activity will be nearby (left, black line) whereas for a selector model even similar actions will have distant representations (right, long black line). **C**, neural activity in both cortex (upper plot) and striatum (lower plot) has complex dynamics of activity with neurons tuned to many different lags and moments of the reach-to-grasp performance. **D**, we simulated the specification model (described in Methods) for two similar actions. PSTHs are aligned to highlight the dominant temporal structure with harder to observe differences as a function of action A and B. **E**, The mean response profile over time for all units. **F**, the mean response profile averaged over all units in the encoding models. **G**, Illustrative population dynamics projected onto the leading principal components (PC1-PC3) for the specification and selector models for actions with a large angle and those with a small angle (plots as labeled). Numbers indicate the normalized Procrustes rotation required to map activity from action A onto action B. **H**, Note that only the specification model predicts small rotations for similar actions. See text and Methods for additional details.

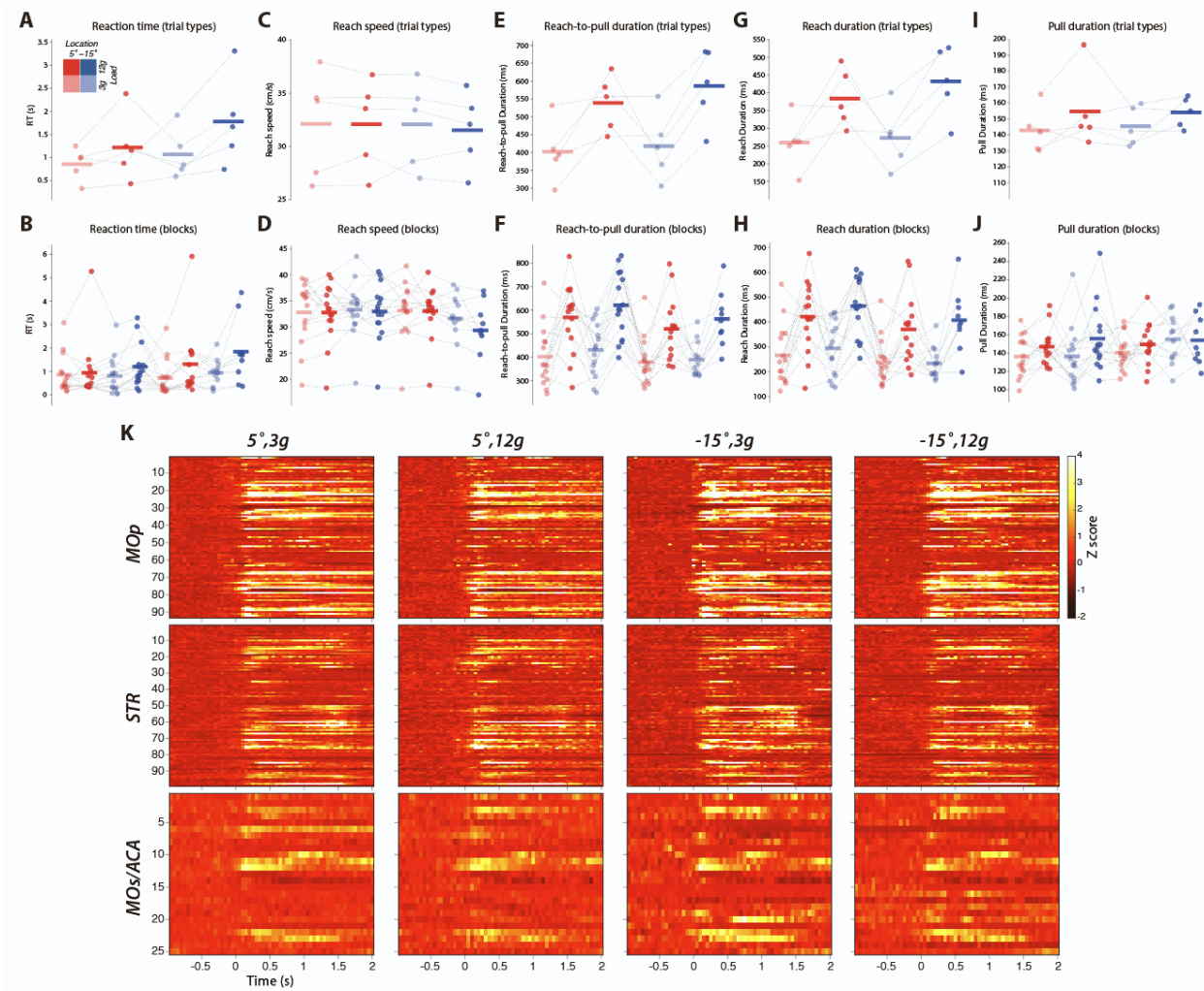


**Figure S2. Characterization of movement kinematics and trial-averaged neural population activity across trial types and blocks, related to Figure 2 and 4.**

**A**, Reaction time (RT) was measured as the latency from the placement of the joystick in the set position (trial start) to the reach start. Each data point represents the average RT of one mouse ( $N=5$ ) for each trial type. There was a trend towards a trial-type-dependent effect (repeated-measures ANOVA;  $F_{3,12}=3.21, P=0.08$ ), as mice increased RTs in blocks with higher joystick loads. Horizontal bars represent the mean across data points. **B**, RTs of all 15 sessions and 8 blocks are plotted to examine change over time in a session due to factors such as satiation and fatigue. **C**, Each data point represents the max reach speed of one mouse averaged across trials and sessions. Mice showed comparable max reach speed regardless of trial types (repeated-measures ANOVA;  $F_{3,12}=0.15, P=0.93$ ). **D**, The max reach speed of all 15 sessions and 8 blocks are plotted. **E-F**, Reach-to-pull duration was measured as the time elapsed from reach start to pull end. We observed a significant effect of trial types (repeated-measures ANOVA;  $F_{3,12}=7.63, P=0.008$ ), as it took more time for mice to complete the reach-to-pull actions in trials with higher joystick loads. This joystick load-dependent effect was consistently observed across sessions and blocks in F. **G-J**, To further analyze the increase in reach-to-pull duration we separately plotted reach (G-H) and pull (I-J) durations. Reach duration was defined as the time elapsed between reach start and pull start. Pull duration was defined as the time elapsed between pull start and pull end. We observed a significant effect of trial types for reach duration (repeated-measures ANOVA;  $F_{3,12}=6.24, P=0.014$ ), but not for pull duration ( $F_{3,12}=1.47, P=0.29$ ). Further analysis suggested that the significant effect observed for reach duration was due to the time taken to overcome the applied counterforce in higher joystick load trials. **K**, Trial-averaged normalized firing rates (z score) of simultaneously recorded MOp, STR, and MOs/ACA populations (rows) for each trial type (columns) from a representative session. Only the trials with successful reach-to-pull performance were included. Each row of heat maps represents the activity of each neuron temporally aligned to the reach start at time=0.

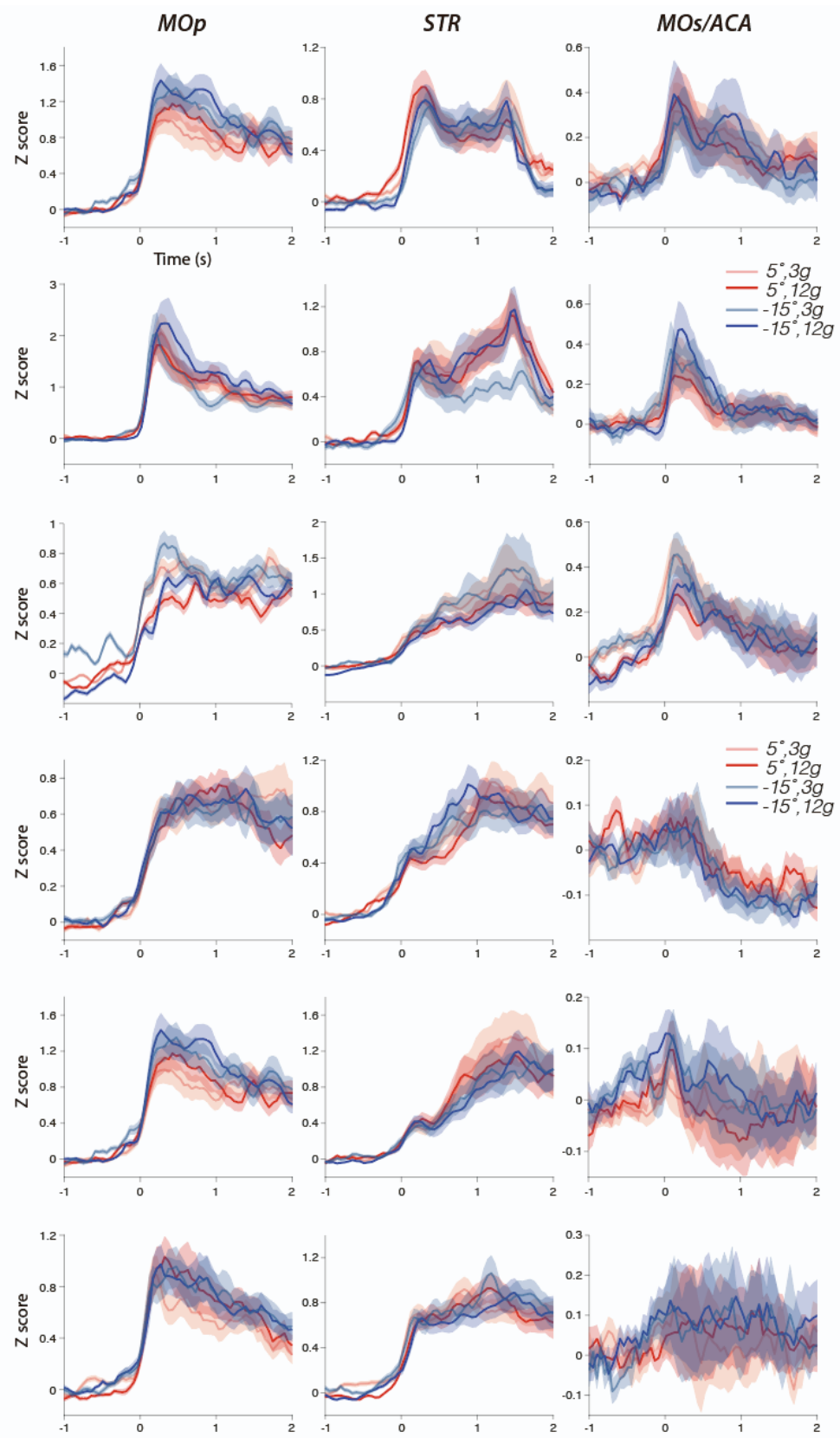


**Figure S3. Z-score normalized activity of all neural populations across four different trial types, related to Figure 4.**

Normalized firing rates (Mean  $\pm$  SEM) of simultaneously recorded MOp, STR, and MOs/ACA populations (columns) were averaged across neurons and plotted separately for each trial type (color-coded). Only the trials with successful reach-to-pull performance were included. All PETHs were temporally aligned to the reach start at time=0.

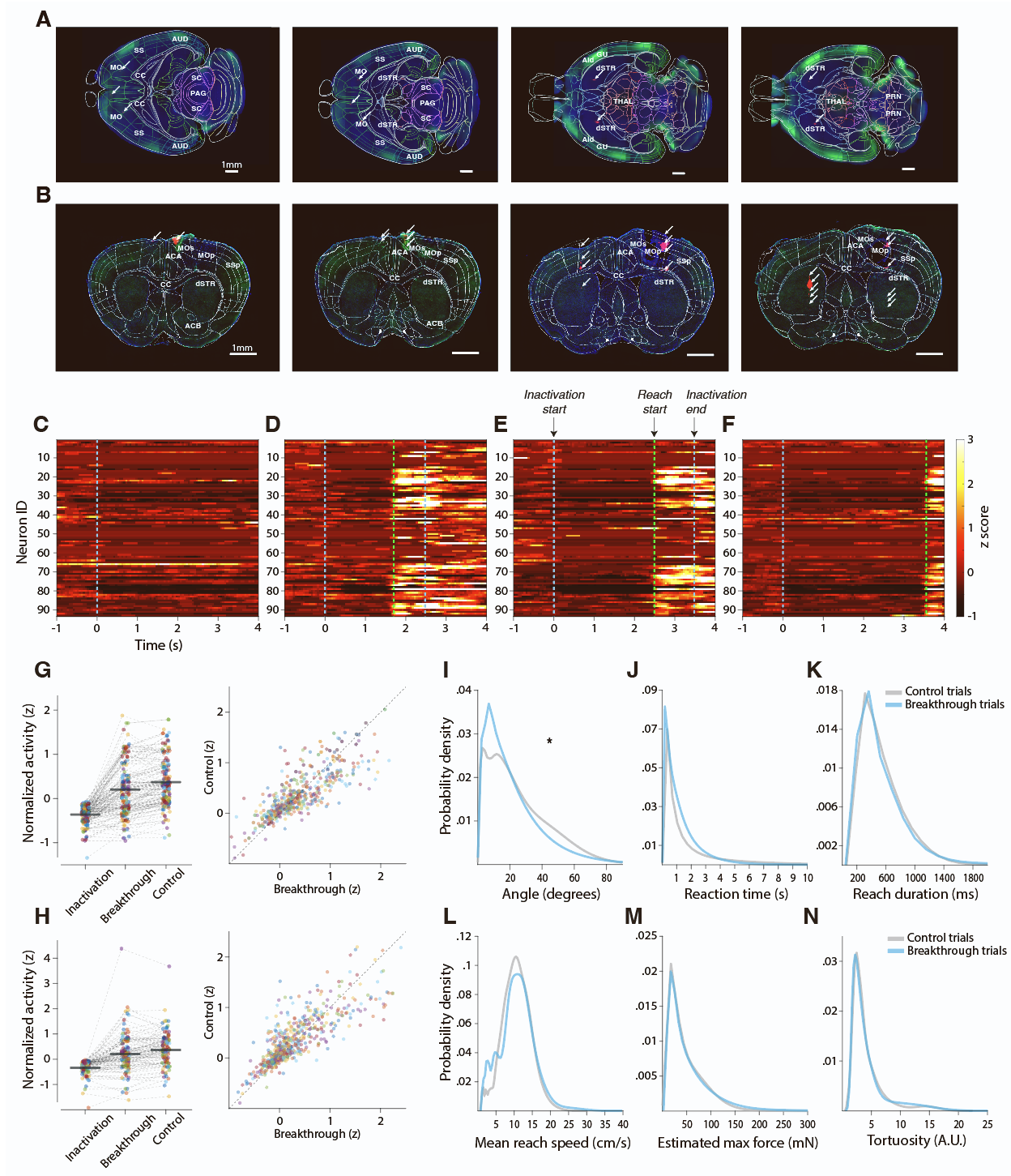


**Figure S4. Impact of corticostriatal neuronal inactivation on reach-to-pull performance, related to Figure 3.**

**A**, Histological reconstruction of the probe track labeled with DiI (highlighted in red, marked with white arrows) superimposed with DAPI (in blue). The presence of eGFP (in green) signifies the expression of GtACR2 for optogenetic silencing. Four exemplary horizontal sections are presented in order from dorsal (left) to ventral (right). **B**, Histological reconstruction in representative coronal sections arranged from anterior (left) to posterior (right). The color scheme matches that of **A**. **C-F**, Example MOp neural population responses aligned to the onset of corticostriatal inactivation ( $t=0$ ). A subset of neurons exhibited clear suppression in their firing rates starting at the laser onset. **C**, Example trial without a breakthrough response. **D-F**, Example trials with breakthrough reach-to-pull responses. Reach onset is marked with a dotted green line. Successful trial completion before the inactivation duration turned the laser off (the second dotted light blue line). **G-H, Left**, Baseline normalized neuronal activity of MOp (G) and STR (H) during the cortical inactivation, breakthrough reaches under inactivation, and control reaches without inactivation. **Right**, Comparison of neuronal activity during reaching with (breakthrough trials; x axis) or without cortical inactivation (control trials; y axis). For simplicity, only neurons exhibiting significant activity suppression during cortical inactivation were included. **I-N**, Characterizing breakthrough movement properties in comparison to control reach-to-pull movements. **I**, Distribution of absolute reach angles during control (gray) and breakthrough (blue) trials. The distribution of reach angles was estimated using a kernel density estimation (KDE) method, which generated smooth curves from the angle data for each trial type. Breakthrough reaches were significantly contracted towards the  $0^\circ$  line, while reaches in the control trials exhibited greater lateralization. **J-N**, Reaction times (J), reach duration (K), reach speed (L), max force (M), and tortuosity (N) across the control and inactivation trials were similar.

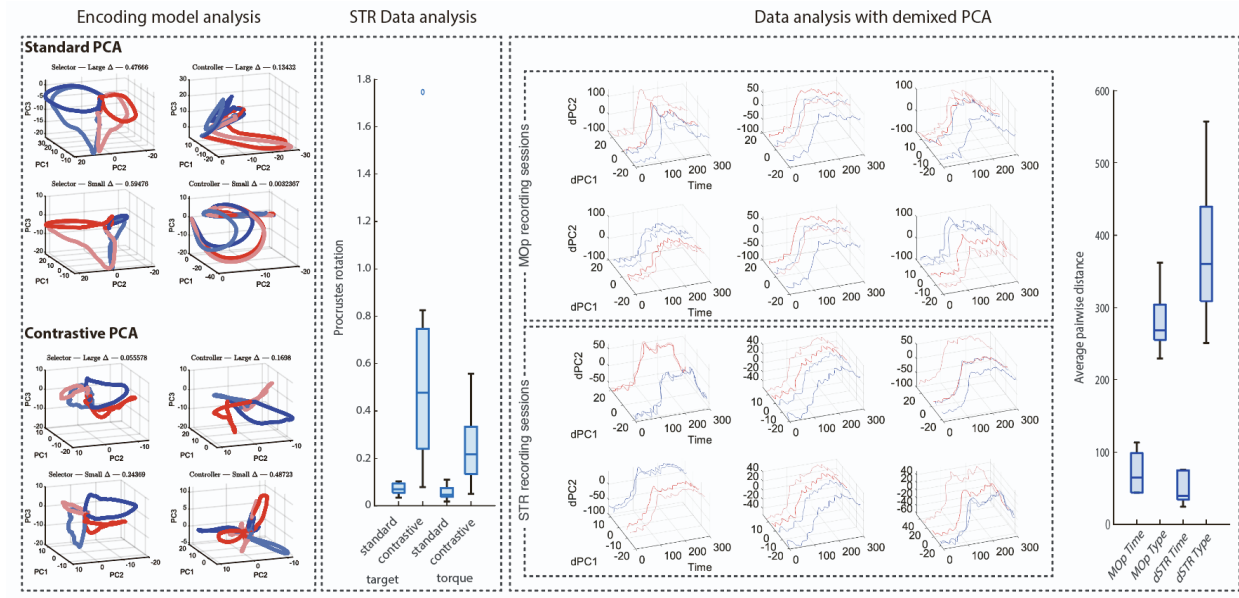


**Figure S5. Differential activity patterns that can be revealed by cPCA, related to Figure 5.**

**Left column (Encoding model analysis),** The encoding model from Figure S1 can be used to provide ground truth for the conjecture that contrastive PCA can reveal separation in population dynamics as a function of action, even from small actions that differ little in the underlying parameters/encoding. Upper panels show standard PCA projection for example model run. Lower panels show contrastive PCA projection for analogous model runs. **Middle column (Procrustes rotation),** We quantified the inter-target and inter-torque rotations of standard and contrastive PCA trajectories using Procrustes rotation. This analysis demonstrates cPCA's effectiveness in capturing distinct neural population responses related to target location and required torque. Full quantification of distribution of rotation values shown in main text and Figure 4D. **Right column (demixed PCA),** dPCA serves as an alternative approach that captures the encoding of task variables while preserving the rich temporal dynamics within neural population activity. The top six and bottom six panels display the mean MOp and STR neural population activities for the four target location and joystick load combinations, projected onto two dPC dimensions. We quantified the average pairwise distance across the neural trajectories for the four trial types and contrasted this distance metric against the trial-type-independent temporal component shared across trial types.

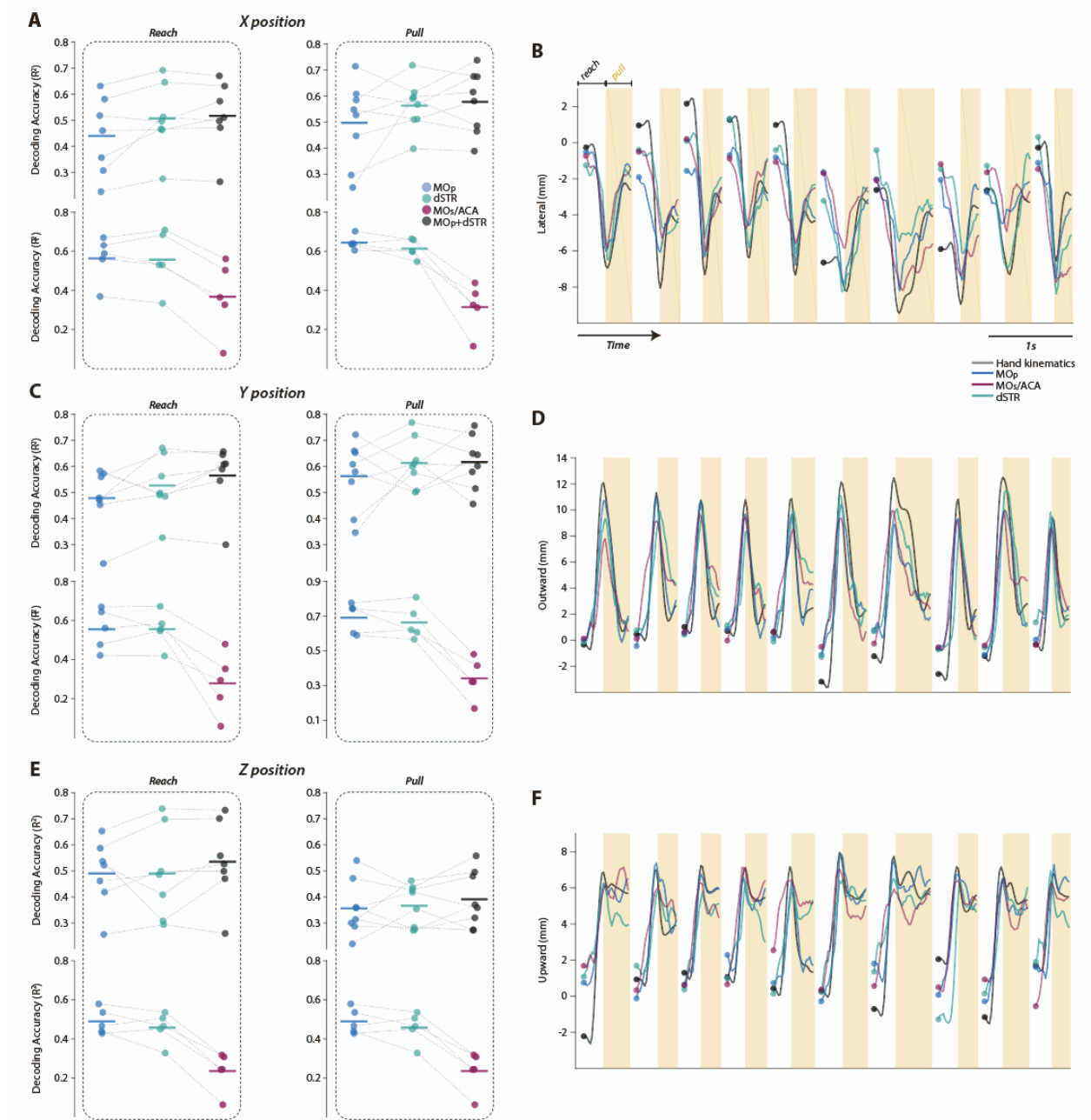


**Figure S6. Continuous decoding of 3D hand trajectories, related to Figure 5.**

The Kalman filter was used to decode 3D hand trajectories based on the neural peri-movement responses with cross-validation and resampling to match the number of neurons across regions. **A**, Decoding accuracies ( $R^2$ ) for hand trajectories along the x axis (left-right) were compared across regions during reach and pull phases. **B**, Ten representative hand trajectories on the x axis decoded from each region were superimposed with the observed hand trajectories (black). **C**, Formatted same as **A** but accuracies are of trajectories on the y axis (forward-backward). **D**, Formatted the same as **B** but trajectories represent hand positions on the y axis. **E**, Formatted same as **A** but accuracies are of trajectories on the z axis (upward-downward). **F**, Formatted the same as **B** but trajectories represent hand positions on the z axis.

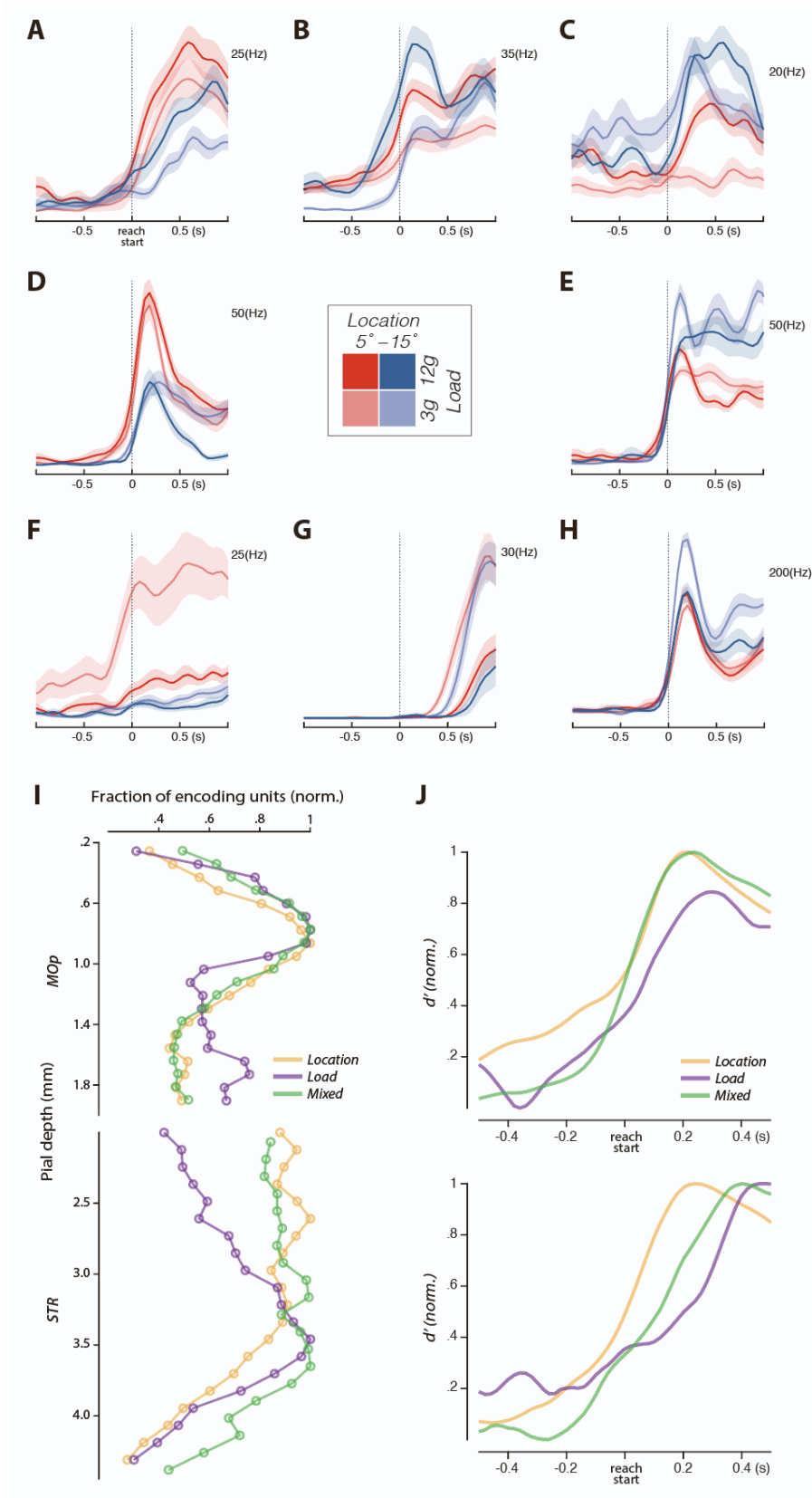


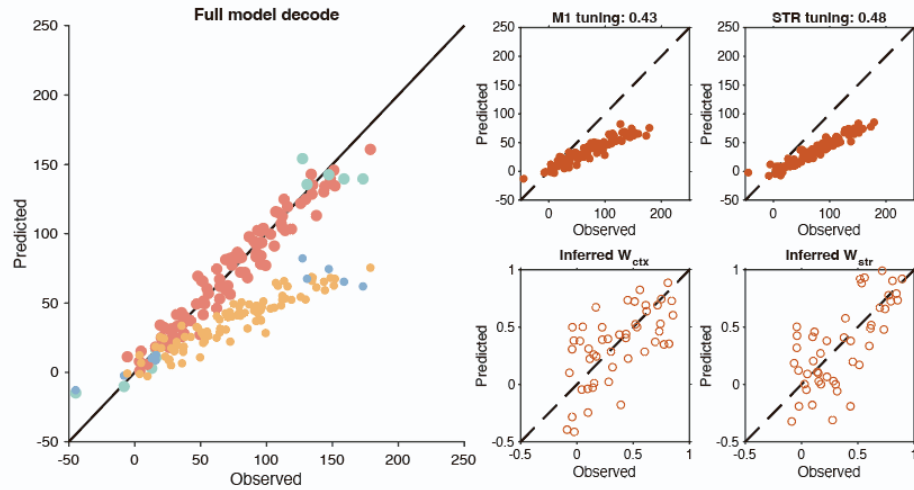
**Figure S7. More details on MOp and dSTR single neuron encoding of trial conditions, related to Figure 6.**

**A-H**, Individual neurons were characterized by their responses to joystick location and load combinations. **A**, An example neuron with preferred response to both leftward location and high joystick load. **B**, An example neuron with preferred response to high load with little sensitivity to target location. **C**, An example neuron with preferred response to both rightward location and high load. **D**, An example neuron with preferred response to leftward target location with little sensitivity to load. **E**, An example neuron with preferred response to rightward target location with little sensitivity to load. **F**, An example neuron with preferred response to both leftward location and high load. **G**, An example neuron with preferred response to low load with little sensitivity to target location. **H**, An example neuron with preferred response to both rightward location and low load. **I-J**, Some individual neurons purely encoded joystick ‘location’ (**D & E**) or ‘load’ (**B & G**), whereas other neurons displayed ‘mixed’ encoding of both (**A, C, F, H**). The spatiotemporal distribution of the three encoding types were examined. **I**, Spatial distribution of ‘location’, ‘load’, and ‘mixed’ encoding neurons along the corticostriatal depth. Fractions of encoding neurons were normalized to the maximum fraction of each encoding group. **J**, Temporal response properties of the three encoding groups. The  $d'$  scores were normalized to the maximum score of each encoding group.

Supplemental Figure 8

## Random $W_{m,s}$ connectivity; equal contribution

Decoding performance and recovery of  $W$  for example simulation



## Activity correlation as a function of $W_{m,s}$ connectivity

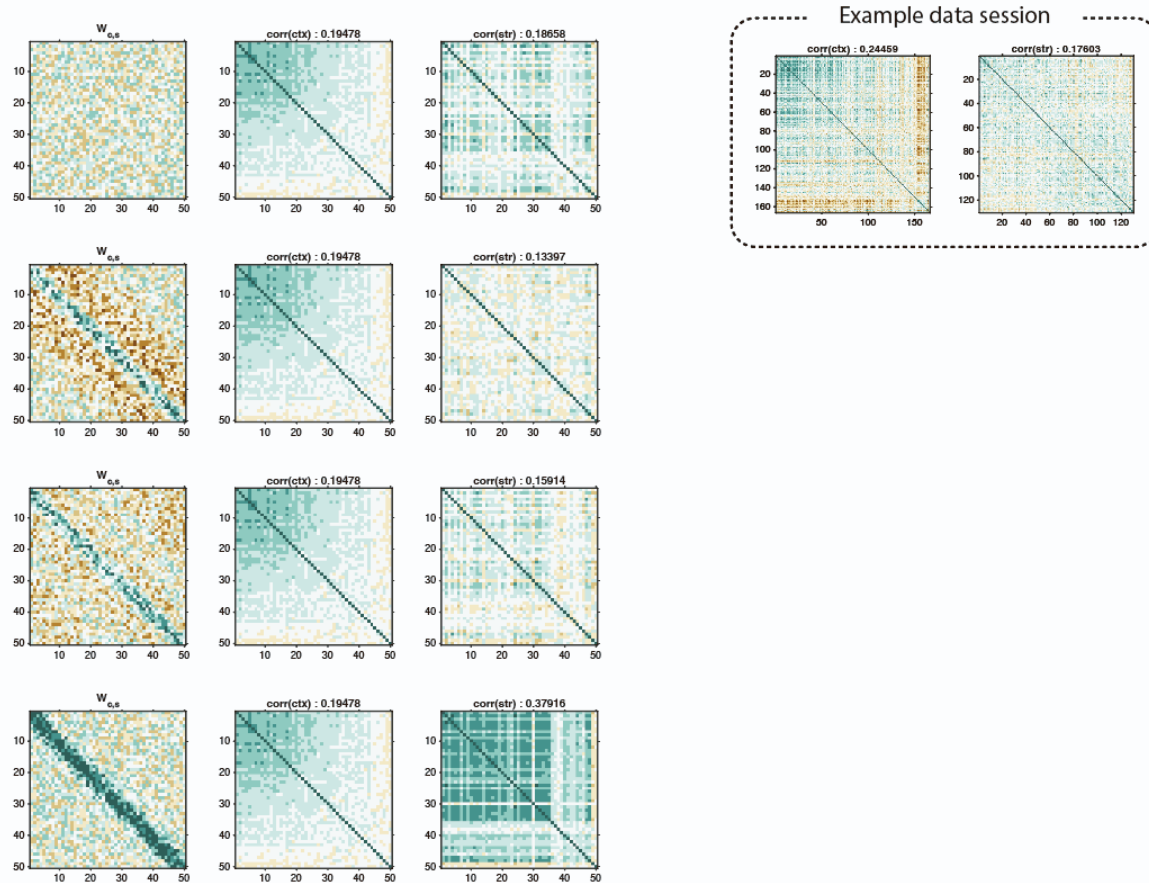


**Figure S8. Elaboration on the 2 layer encoding model details, related to Figure 8.**

The 2 layer encoding model described in the main text is sufficient to recover equivalent decoding contributions from motor cortex ('m' layer) and striatum ('s' layer) under the assumption that the two are independent (upper panels). All x-axes are Observed output variables and all y-axes are corresponding Predicted values of the same variables from the decoding procedure. Left and upper panels are observed movement force from separate and joint decoding. Independent decoding (upper, left MOp; upper, right STR) where tuning refers to the slope between Predicted and Observed. Lower panels in the top section illustrate the recovered weight matrix ( $W_{ctx}$ ) coupling 'm' output and weight matrix ( $W_{str}$ ) coupling 's' layer directly to predict movement force variable. Decoding from activity and observed output values approximately accurately recovers these unobserved coupling weights. Lower section: To illustrate how expected striatal activity ('s') correlations vary as a function of cortex->striatum coupling weights ( $W_{m,s}$ ) pairwise correlation matrices are plotted for random (top), center\_surround (second), distributed center surround (third, used for calculations in main text), and topographic excitatory (bottom). An example data session pairwise correlations of integrated response during pull phase correlations are shown at right (distribution shown in main text).

Supplemental Table 1

Mouse ID	The number of training sessions to reach the criterion	The number of behavioral sessions included in the dataset	The number of behavioral + neural recording sessions included in the dataset	The number of corticostriatal inactivation sessions included in the dataset
M25	40	0	0	0
M28	35	0	0	0
M37	28	4	1	2
M38	23	4	4	3
M39	24	4	1	3
M40	20	2	2	3
M44	10	1	1	0
M45	20	0	0	1
M46	16	0	0	0
M47	N.A.	0	1	0
M48	N.A.	0	1	0

**Table S1. Details of training history for each mouse, related to Figure 2**

Detailed usage data from each animal is listed. The second column indicates the number of training sessions required for each animal to reach the training completion criterion (Figure 2E). The third column specifies the number of sessions included in the dataset used to characterize the movement kinematics and kinetics (Figures 2F-H and S2). The fourth column shows the number of sessions with simultaneous behavioral monitoring and neural recording (Figures 4-6, 8, S2, S3, and S4). The fifth column indicates the number of sessions used to examine the behavioral and/or neural impact of corticostriatal inactivation (Figures 3-4 and S4I-N). To examine the relative contribution of MOp and STR over the course of learning we trained an additional pair of mice (M47, 48). They were kept on different training and experimental protocols, and their data were used only for Figure 8.